# Monte Carlo design studies for the Cherenkov Telescope Array

K. Bernlöhr [a,b,*], A. Barnacka [c], Y. Becherini [d,e], O. Blanch Bigas [f], E. Carmona [g,h], P. Colin [g], G. Decerprit [i,j], F. Di Pierro [k], F. Dubois [l], C. Farnier [m,n], S. Funk [o], G. Hermann [a], J.A. Hinton [p], T.B. Humensky [q], B. Khélifi [d], T. Kihm [a], N. Komin [r], J.-P. Lenain [s,t], G. Maier [i], D. Mazin [f,g], M.C. Medina [u], A. Moralejo [f], S.J. Nolan [v], S. Ohm [p,w], E. de Oña Wilhelmi [a], R.D. Parsons [w,a], M. Paz Arribas [i,b], G. Pedaletti [x], S. Pita [e], H. Prokoph [i], C.B. Rulten [v], U. Schwanke [b], M. Shayduk [i], V. Stamatescu [f], P. Vallania [k], S. Vorobiov [y,i], R. Wischnewski [i], T. Yoshikoshi [z], A. Zech [t], for the CTA Consortium

[a] Max-Planck-Institut für Kernphysik, P.O. Box 103980, D-69029 Heidelberg, Germany
[b] Institut für Physik, Humboldt-Universität zu Berlin, Newtonstr. 15, D-12489 Berlin, Germany
[c] Nicolaus Copernicus Astronomical Center, Polish Academy of Sciences, ul. Bartycka 18, 00-716 Warsaw, Poland
[d] Laboratoire Leprince-Ringuet, Ecole Polytechnique, CNRS/IN2P3, F-91128 Palaiseau, France
[e] Astroparticule et Cosmologie (APC), CNRS, Université Paris 7 Denis Diderot, Paris Cedex 13, France
[f] Institut de Fisica d'Altes Energies (IFAE), Edifici Cn., Campus UAB, E-08193 Bellaterra, Spain
[g] Max-Planck-Institut für Physik, Föhringer Ring 6, D-80805 München, Germany
[h] Centro de Investigaciones Energéticas, Medioambientales y Tecnológicas (CIEMAT), Madrid, Spain
[i] DESY, Platanenallee 6, D-15738 Zeuthen, Germany
[j] Argonne National Laboratory, 9700 S. Cass Avenue, Argonne, IL 60439, USA
[k] Osservatorio Astrofisico di Torino dell'Istituto Nazionale di Astrofisica, Corso Fiume 4, I-10133 Torino, Italy
[l] Universidad Complutense, E-28040 Madrid, Spain
[m] Department of Physics, Stockholm University, AlbaNova, SE-106 91 Stockholm, Sweden
[n] The Oskar Klein Centre for Cosmoparticle Physics, AlbaNova, SE-106 91 Stockholm, Sweden
[o] Kavli Institute for Particle Astrophysics and Cosmology, SLAC, Stanford, CA 94025, USA
[p] Department of Physics and Astronomy, The University of Leicester, Leicester LE1 7RH, United Kingdom
[q] Physics Department, Columbia University, New York, NY 10027, USA
[r] LAPP, Université de Savoie, CNRS/IN2P3, F-74941 Annecy-le-Vieux, France
[s] Landessternwarte, Universität Heidelberg, Königstuhl, D-69117 Heidelberg, Germany
[t] LUTH, Observatoire de Paris, CNRS, Université Paris Diderot, 5 place Jules Janssen, F-92190 Meudon, France
[u] CEA Saclay, DSM/IRFU, F-91191 Gif-Sur-Yvette Cedex, France
[v] University of Durham, Department of Physics, South Road, Durham DH1 3LE, United Kingdom
[w] University of Leeds, School of Physics and Astronomy, Leeds LS2 9JT, United Kingdom
[x] Institut de Ciències de l'Espai (IEEC-CSIC), Campus UAB, Torre C5, E-08193 Barcelona, Spain
[y] LUPM, UMR 5299 Université Montpellier II & IN2P3/CNRS, F-34095 Montpellier, France
[z] Institute for Cosmic Ray Research, The University of Tokyo, Kashiwa, Chiba 277-8582, Japan

### ARTICLE INFO

### ABSTRACT

The Cherenkov Telescopes Array (CTA) is planned as the future instrument for very-high-energy (VHE) gamma-ray astronomy with a wide energy range of four orders of magnitude and an improvement in sensitivity compared to current instruments of about an order of magnitude. Monte Carlo simulations are a crucial tool in the design of CTA. The ultimate goal of these simulations is to find the most cost-effective solution for given physics goals and thus sensitivity goals or to find, for a given cost, the solution best suited for different types of targets with CTA. Apart from uncertain component cost estimates, the main problem in this procedure is the dependence on a huge number of configuration parameters, both in specifications of individual telescope types and in the array layout. This is addressed by simulation of a huge array intended as a superset of many different realistic array layouts, and also by simulation of array subsets for different telescope parameters. Different analysis methods – in use with current installations and extended (or developed specifically) for CTA – are applied to the simulated data sets for deriving the expected sensitivity of CTA. In this paper we describe the current status of this iterative approach to optimize the CTA design and layout.

* Corresponding author at: Max-Planck-Institut für Kernphysik, P.O. Box 103980, D-69029 Heidelberg, Germany.
E-mail address: Konrad.Bernloehr@mpi-hd.mpg.de (K. Bernlöhr).

## 1. Introduction

The concept of the Cherenkov Telescope Array (CTA) [1,2] is based on a straightforward expansion of current imaging atmospheric Cherenkov telescope (IACT) arrays for very high energy (VHE) gamma-ray astrophysics such as H.E.S.S., MAGIC, and VERITAS [3–5]. It aims to improve the current sensitivity by an order of magnitude and extend the current sensitive energy region to lower and higher energies covering a range of about four orders of magnitude. In order to study astrophysical objects in such a wide energy range, CTA will consist of at least three different sized telescopes: the Large Size Telescopes (LSTs, ∼24 m aperture) will record showers with energies as low as ∼20 GeV, the Medium Size Telescopes (MSTs, ∼12 m aperture, later to be supplemented by SC-MSTs of 9 m aperture with Schwarzschild–Couder (SC) optics [6]) will operate in the ∼1 TeV range, and the Small Size Telescopes (SSTs, ∼4–7 m aperture) are optimized for high energies up to more than 100 TeV. This design scenario is schematically shown in Fig. 1 of the CTA Design Concepts [7] and possible implementations are illustrated in Section 6 of the current paper. The performance of an IACT array is also determined by quantities like the angular resolution, energy resolution or sensitive field of view (f.o.v.). These performance estimators depend on a large number of technical and design parameters within a cost envelope. The role of the Monte Carlo (MC) Work Package (WP) of CTA is to optimize the array configuration in this parameter space using MC simulations, given scientific requirements as suggested by the Physics (PHYS) WP.

Our extensive simulation studies to optimize the CTA design are also motivated by several earlier simulation studies, in the following separated into three energy regimes. In the **low energy regime**, from 100 GeV down to a few GeV in the most extreme proposals, it is essential to collect more Cherenkov photons from a gamma-ray shower with a very large aperture telescope of the 20–30 m scale and/or at a very high altitude of ≳4000 m. ECO-1000 (European Cherenkov Observatory, with a mirror surface of 1000 m$^2$) has been the most extreme proposal in terms of mirror area of a single telescope [8]. On the basis of the former ideas, a large single telescope of 34 m aperture with high quantum efficiency photon detectors in the focal plane for a further light gain was proposed. The large proposed aperture and efficiency raises major noise problems. Simulation studies for such a huge telescope show that night sky background (NSB) light collected by the large reflector causes high accidental trigger rates and a smaller pixel size is preferable to reduce this effect. In addition, Cherenkov light from single secondary muons arriving at large distances of ≳40 m results in gamma-ray-like images which cannot be rejected completely by a single tele-

scope. The latter noise due to single muons can be eliminated by stereoscopic IACT arrays. An array of 30 m telescopes was proposed [9] for a 10 GeV threshold at 1800 m altitude. Another proposed project, 5@5, was intended as an array of 4–5 IACTs of ∼20 m aperture, aiming at a threshold as low as ∼5 GeV gamma rays at a very high altitude site of about 5 km a.s.l. [10]. This low threshold at high altitude can be achieved because, being closer to shower maximum, the Cherenkov light is less diluted – but at the cost of smaller effective areas and more difficult gamma-hadron separation when electrons in most gamma-ray showers reach the telescopes.

Cherenkov telescopes should focus light coming from a distance $d$ (typical distance of the average shower maximum) onto the pixels. If defocusing by half of a pixel diameter $p$ is acceptable, the depth of field is then from about $d/(1 + pd/(2fD))$ to $d/(1 - pd/(2fD))$ (or infinity if $pd \geqslant 2fD$), with focal length $f$ and telescope diameter $D$. While the depth of field of small Cherenkov telescopes encompasses most showers entirely, a problem with large telescopes – particularly severe at high altitude – is the very limited depth of field, unable to focus all parts of shower images at the same time [11]. The useful size of large Cherenkov telescopes is thus not just limited by their cost and CTA does not plan to build extremely large telescopes.

In the **medium energy regime** from about 100 GeV to some 10 TeV, CTA aims to improve the sensitivity by stereoscopic observations using several IACTs simultaneously. A previous simulation study of a dense IACT array (33.3 m telescope spacing) shows that the angular resolution $\sigma$ depends on the number of telescopes $N$ used in the reconstruction and is improved as $\propto N^{-1/2}$ up to $N \sim 50$ [12]. The point-source sensitivity is limited by background fluctuations in this energy regime and approximately proportional to $\sigma A^{-1/2} Q^{-1}$, where $A$ is the effective area and $Q = \epsilon_\gamma/\sqrt{\epsilon_{bg}}$ is the quality factor usually defined in terms of the gamma-ray and background cut efficiencies $\epsilon_\gamma$ and $\epsilon_{bg}$, respectively. There is a trade-off between $\sigma$ and $A$ since the number of available telescopes is limited by the cost. However, high telescope-multiplicity observations also give better background rejection and thus a larger $Q$.

In the **high energy regime** beyond some 10 TeV, an extensive IACT array called TenTen has been proposed aiming to achieve a 10 km$^2$ effective area at energies greater than 10 TeV [13]. It consists of relatively small IACTs of 3–5 m aperture located with an inter-telescope spacing of ≳300 m. This sparse array design, which was first suggested by Plyasheshnikov et al. [14], enables less IACTs to expand the effective area cost-effectively. The IACTs are also required to have a larger f.o.v. diameter of ≳8° as they detect Cherenkov photons at large core distances beyond the plateau area of the Cherenkov light pool (radius ∼120 m). Also there, the Cher-
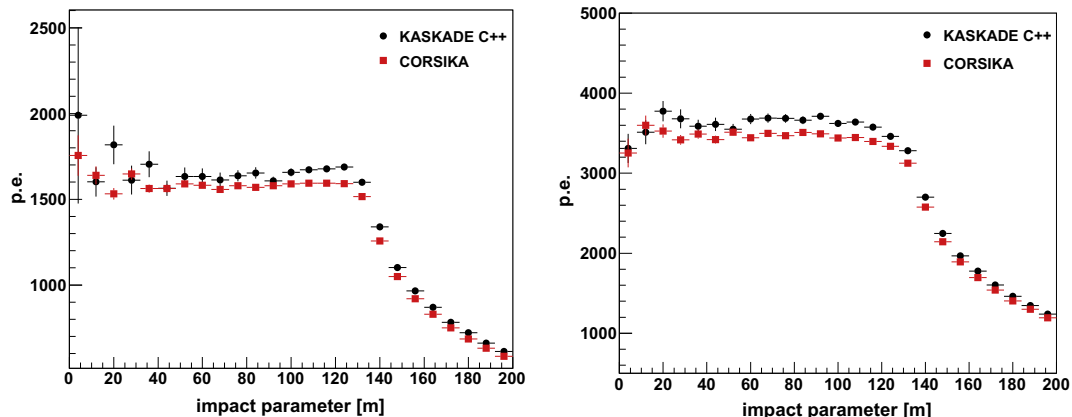


**Fig. 1.** Simulated Cherenkov light profiles (in p.e. collected by the camera on a 106 m$^2$ H.E.S.S. telescope [24,25]) for vertical gamma-ray showers at 500 GeV (left) and 1 TeV (right) for CORSIKA and KASKADE-C++, as a function of the impact parameter. No atmospheric extinction of the Cherenkov light has been applied.

enkov photon density sharply drops with increasing the core distance, with consequences on the energy threshold and also on the accuracies of determining the arrival direction and the core position (see [15] on the optimization of an IACT array). The stereoscopic reconstruction can also be complemented using the time gradient analysis [16]. Also, the simulation study by de la Calle Pérez and Biller [17] indicates that the sensitivity can be improved by more than three times above 300 GeV and significantly more than this above 10 TeV, only by using a wide f.o.v. camera of 10° diameter with a conventional telescope spacing.[2]

The above mentioned ideas and many technical aspects should be considered in the Monte Carlo simulation study for CTA. The optimization of the array configuration within such a large parameter space is thus a challenging task. Before the detailed CTA design study, preliminary simulations have been carried out with some homogeneous and graded array configurations, focusing mainly on the low to medium energy range [18], which demonstrated that the CTA goal sensitivity can be achieved within an anticipated budget.

So far, only single mirror optics such as the parabolic or Davies–Cotton (DC) designs have been used for IACTs, although secondary mirrors are commonly used in optical telescopes in order to get much better spot sizes correcting the spherical and coma aberrations. The AGIS (Advanced Gamma-ray Imaging System) group [19], now part of CTA, proposed an advanced idea utilizing a two mirror optics called the Schwarzschild–Couder optics for IACTs [6]. With these optics, IACTs can have a very large f.o.v. up to ∼15° without significant degradation of the spot size and therefore increase survey capabilities with a good angular resolution. These optics possibly give some other advantages: the physical pixel size is more compact than that of the single mirror optics and cost-effective photon sensors such as multi-anode photomultiplier tubes (MAPMTs) or silicon photomultipliers (SiPMs) can be used for the camera. Moreover, the physical telescope length along the optical axis gets shorter and the cost of the telescope structure can be reduced significantly. On the other hand, requirements on the optical quality get more ambitious. A portion of CTA (mainly US groups, following up on the AGIS project) aims to complement the baseline CTA design with a sub-array of 9.5 m diameter SC-MSTs. The SC design is also attractive for the SST array because of its wide f.o.v. capability, which is needed for the sparse telescope array concept. Two different optical designs for 4 m SC-SSTs and two different camera concepts for them are under development.

In this paper, we describe our detailed simulation study for CTA carried out after [18]. In Section 2, details of the software tools used for our simulation study are summarized. Our simulation work is an integration of several activities in this field and various data analysis methods are simultaneously considered and developed. We describe details of the analysis methods in Sections 3 and 4. The interface to and tools for the physics program of CTA are summarized in Section 5. The common array configurations used in the mass production of simulation data are presented in Section 6. Our current results of performance estimations for candidate arrays with the baseline analysis are described in Section 7 and compared with those of the other analyses in Section 8. We describe future directions of our study in Section 9 and conclude in Section 10.

## 2. Monte Carlo simulation tools

### 2.1. Air shower simulation

The first step in the generation of very high energy (VHE) gamma-ray events or background (cosmic ray) events for CTA is the simulation of the extensive air shower, i.e. the cascade of secondary particles developing in the atmosphere. Several codes exist for the detailed, three-dimensional MC simulation of air showers for different primary particles. A MC simulation of the shower development, rather than an analytical solution of the cascade equations, is necessary to correctly account for statistical fluctuations between showers. The main challenge of these simulations is the correct treatment of hadronic interactions, which play a central role in the development of air showers triggered by cosmic rays. Phenomenological models are used to extrapolate cross-sections beyond the energy regime and scattering angles accessible to accelerator experiments.

The air shower generator CORSIKA [20] has been chosen as a standard tool for CTA simulations. This publicly available, open-source code is used by all the current IACT arrays and represents a standard tool in the wider astroparticle physics community. While electromagnetic interactions in CORSIKA are treated by an adapted version of the EGS4 code [21], a choice is given between several hadronic interaction models. The "IACT/ATMO" package [22] facilitates the simulation of the Cherenkov light flux for a chosen configuration of telescope positions and dish sizes. The flux of Cherenkov photons from a simulated air shower is collected for each pre-defined telescope position and dish size and serves as input for further processing with a telescope simulation package.

The generation of proton-induced showers, needed for background estimations, largely dominates the CPU time and requires substantial amounts of memory and disk space. The large volume of simulations needed to investigate all the different configurations for the array has motivated the use of the EGEE/EGI (Enabling Grids for E-sciencE/European Grid Initiative) Computing Grid for the massive production of shower and detector simulations, in addition to the use of local computing resources. Within the Grid virtual organization for CTA, 14 computing centers located at collaborating institutes provide computing power and storage. To save disk space and CPU time, the output of CORSIKA is usually piped directly into several instances of the telescope simulation software to generate the response of different array configurations in parallel, without writing the large CORSIKA output files to disk. At peak times of MC production, up to 2000 simulation jobs can run in parallel. The large distributed data storage space (several 100 TB on disks and tapes) makes it also possible to temporarily store CORSIKA files for later reprocessing, to compare for example the same showers as seen with different night sky background or for different telescope implementation details. It is foreseen to equally perform the further processing and analysis of the simulated data on the Computing Grid in the near future. In addition, massive simulations have been carried out on local CPU clusters at several CTA member institutes and the data are provided for download and were used for the baseline analysis as well as for some of the alternative analyses.

The Cherenkov light production from gamma-ray events simulated with CORSIKA has been cross-checked against another air shower generator (KASCADE-C++) currently in use within the H.E.S.S. collaboration. This code had been developed by the ARTEMIS-Whipple, CAT, and H.E.S.S. collaborations, based on the original KASCADE code [23]. The Cherenkov light profile generated by the two air shower codes agrees to within ∼5% (cf. Fig. 1), resulting in consistent telescope trigger rates and photo-electron (p.e.) distributions in the camera.

The simulation of the cosmic ray background is subject to our still limited knowledge of hadronic interaction processes at very high energies. Detailed comparisons of the different interaction models available in CORSIKA can be found in [20] and an evaluation of the systematic uncertainties is given by [26]. The impact on the Cherenkov light profile has been studied for some of the most commonly used interaction models for low and high proton

---

[2] The authors also utilized a time gradient cut and cuts with shower reconstruction parameters (energy and shower maximum height) to improve the sensitivity.

energies. There are no significant differences between the low energy (<80 GeV) models FLUKA [27] and UrQMD [28]. The known discrepancy between the high-energy models QGSJet-01 [29], QGSJet-II [30,31] and SIBYLL 2.1 [32], which apply different extrapolations of interaction parameters to high energies, leads only to a small uncertainty of about 5% in the Cherenkov light profile at 1 TeV. Examples of light profiles are shown for comparison in Fig. 2. UrQMD and QGSJet-II had been chosen for the massive background simulations for CTA.

## 2.2. Cherenkov telescope simulation

The simulation of the detector response includes the optical ray-tracing of the photons from the mirror to the photomultiplier tubes in the camera, the electronics and the digitization of the signals, as well as the trigger system. Noise from the night-sky background and from the electronics need to be added to the signal as well. The telescope simulation package sim_telarray [22], based on software developed for HEGRA and now in use by the H.E.S.S. collaboration, is employed for the massive simulations for CTA. In general, sim_telarray requires only a small fraction of the CPU time needed for shower simulations. Once an air shower has been simulated by CORSIKA and processed through sim_telarray, only the final output is written to disk.

The simulation of the CTA instrumental response has been cross-checked with the SMASH software [33], which is also used within the H.E.S.S. collaboration, and with the code used by the MAGIC collaboration [34]. The agreement with sim_telarray is generally very good. As an example, gamma-ray induced air showers at 1 TeV and with a zenith angle of 30° have been generated with CORSIKA at a distance of about 150 m from the center of a H.E.S.S. type four-telescope array. The distribution of the average signals for 100 simulated showers processed by the two programs is shown in Fig. 3. All of the showers used to generate Fig. 3 have an impact parameter to the simulated telescope of 150 m. A good overall agreement is seen between the detector response simulation provided by the two codes. The apparent differences at large pixel amplitudes result from very few of the simulated events and are not significant.

## 2.3. Verification of the simulation chain against data

The simulation chain for CTA is directly based on programs that are already in use within the H.E.S.S. and MAGIC collaborations and that have been thoroughly tested against real data. Comparisons of
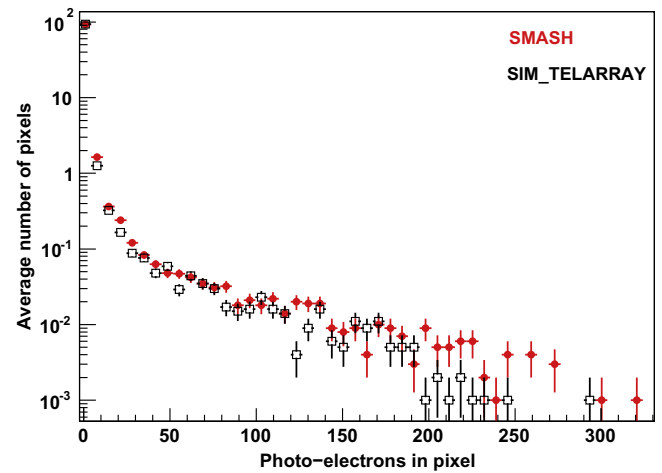


**Fig. 3.** Average number of pixels with a given raw intensity (in units of photoelectrons) for the same 100 simulated air showers seen by SMASH (red filled circles) and sim_telarray (black open squares). (For interpretation of the references to color in this figure legend, the reader is referred to the web version of this article.)

MC events against H.E.S.S. data, verifying for example the distribution of photons in starlight images, the point spread function (PSF) for different angular distances to the optical axis, or the telescope and system trigger rate, have been extensively studied as well as the resulting shower images (e.g. [22,35–37]).

The giant flare detected from the blazar PKS 2155-304 with H.E.S.S. on July 29th, 2006 provided a good opportunity for an end-to-end test of the complete simulation chain for gamma-ray induced showers. The very high signal to background ratio during the flare, which was detected at 168 standard deviations in about 1.5 h of live time, made it appear as an almost pure gamma-ray test beam. For the data-MC comparison, gamma-ray showers were simulated with the CORSIKA and KASKADE-C++ programs and passed through the SMASH detector simulation. The measured spectrum (power law spectral index) during these 1.5 h, the optical efficiency, the zenith angle distribution and other runtime parameters were used as inputs to this simulation to reproduce the exact conditions during data acquisition. One of the standard Hillas-type analysis chains was applied to the real and fake data. Fig. 4 shows the good agreement (typically at the 5% level) between the simulated and detected shape of the shower images, as characterized by their Hillas width and length parameters.
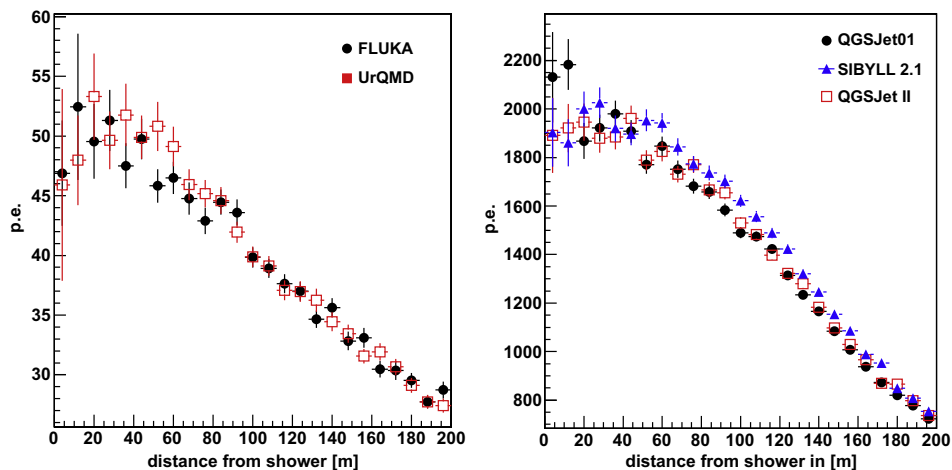


**Fig. 2.** Comparison of the simulated Cherenkov light profiles for vertical proton-induced showers generated by CORSIKA with different hadronic interaction models. The profiles of p.e. collected by a H.E.S.S. camera [24,25] for FLUKA and UrQMD at 100 GeV are shown in the left panel. In the right panel, the high-energy interaction models QGSJet-01c, SIBYLL, and QGSJet-II are compared for showers induced by 1.0 TeV protons, all using URQMD for low-energy interactions.

## 3. Baseline analysis methods

### 3.1. Image cleaning, second moments, and additional parameters

The by now quasi classical analysis method for stereoscopic reconstruction of IACT data is based on the *Hillas parameters* [39], as derived from zeroth order (amplitude or size), first order (center of gravity position), and second order (width, length, orientation) moments of the images. Since these parameters are highly sensitive to the presence of NSB noise, *image cleaning* is applied first, usually in the form of a two-level (or multi-level) procedure [40]. The default two-level procedure requires that a pixel is above a given *high* level and at least one of its neighbors is above a *low* level or vice versa. The *tail-cut levels* of this image cleaning procedure have to be adapted to the NSB level, in order to include enough pixels with significant Cherenkov signals well above the NSB noise level. Typical high (low) levels are 10.0 (5.0) p.e. times the square root of the per-pixel NSB rate in units of photo-electrons per 10 ns.

The calibrated and cleaned images are parametrized by the centroid position ($x_{cog}$, $y_{cog}$) in the camera, the *width* $w$, the *length* $\ell$, and *orientation* $\phi$ parameters of the Hillas ellipse, as well as the amplitude sum $A$ in units of p.e. Use of higher-order moments (skewness, kurtosis) is also possible.

A newer parameter is the *time gradient* along the major axis of the Hillas ellipse. It is obtained from the times when the peak amplitudes are seen in the individual pixels. This time gradient is closely related to the distance of the telescope from the shower axis. It is complemented by pixel time residuals.

### 3.2. Geometric shower reconstruction

In the classical Hillas-parameter stereo reconstruction, the shower direction is determined by a weighted mean of all pairwise intersections of the major axes of two suitable images mapped into a common coordinate system. Suitable here means that images must exceed a given minimum image amplitude in a minimum number of pixels. The images should also not be substantially clipped at the edge of the camera f.o.v. to avoid degraded geometric and energy reconstructions.
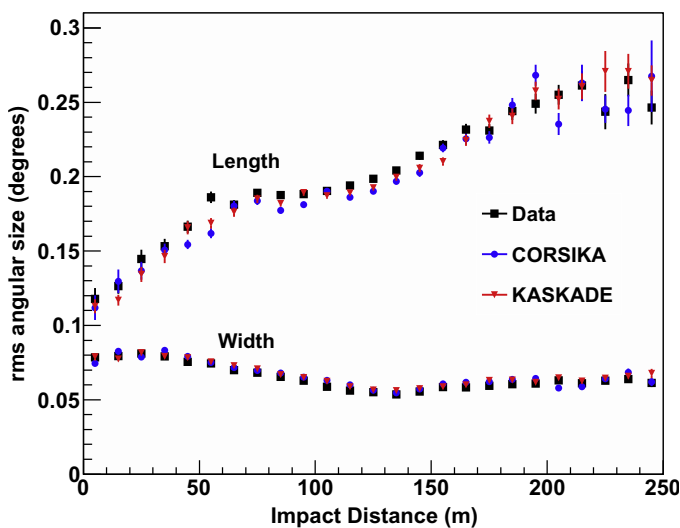
**Fig. 4.** Comparison of measured (black squares) and simulated (red triangles and blue circles) image parameters for the H.E.S.S. telescopes. The real data are taken from a flare of the blazar PKS 2155-304 [38] for which the signal to noise ratio was very high and large gamma-ray statistics are available. (For interpretation of the references to color in this figure legend, the reader is referred to the web version of this article.)

After some experiments, the following weights for intersection pairs were found to result in a significant improvement of the angular resolution over previous weighting schemes:

$$w_{ij} = A_{red}^2 \sin^2(\phi_i - \phi_j)\delta_i^2\delta_j^2, \tag{1}$$

where $A_{red} = A_iA_j/(A_i + A_j)$ is the reduced amplitude of the pair of images and $\delta = 1 - w/\ell$ is a simplified variant of the *disp* parameter [41,42]. The reconstructed shower direction corresponds to the weighted average of all intersection points. The same scheme is also applied to the reconstruction of the shower core location, which is carried out with telescope positions projected into the plane perpendicular to the reconstructed shower direction (the *shower plane*).

The selection of images not (much) affected by edge clipping is always a compromise between the largest possible efficiency and the best possible angular and core position resolution. The current compromise is:

$$r_{cog} < 0.82r_{cam} - 0.35\ell, \tag{2}$$

where $r_{cog}$ is the distance between camera center and the image center-of-gravity, and $r_{cam}$ is the effective radius of the camera, for the almost circular cameras here the same as their geometrical radius. There may be room for improvement here, in particular when taking into account the actual shape of the camera edge. Pixel-based shower fitting schemes are expected to be affected much less by clipped images than our baseline scheme.

The *height of shower maximum* $H_{max}$ or the corresponding *atmospheric depth* $t_{max}$ (the latter measured in g/cm² from the top of the atmosphere along the shower axis) turns out to be of particular importance for low-energy showers where the traditional shape cuts for gamma–hadron discrimination have poor efficiency.

### 3.3. Look-up tables for energy reconstruction and gamma-ray selection cuts

Many of the shower reconstruction and gamma–hadron selection cuts make use of *look-up tables* of the mean values and variances (typically versus two independent parameters) of some resulting parameters obtained from simulated gamma rays. These are obtained from filling a total of four corresponding histograms with (a subset of) the simulated gamma rays, for the number of entries, the sum of event weights (correcting from simulated spectra to assumed source spectra), as well as the sum of the event-weighted parameter and its square.

An example is $E/A$, the ratio of (true) shower energy to (measured) image amplitude, versus core distance $R_c$ (more precisely the distance of the telescope from the shower axis) and $\log_{10}A$ of the telescope. The latter is not only used to obtain estimates of the primary energy for each telescope with a suitable image and the expected error on such an estimate, but also to obtain a weighted mean energy, to check for the consistency of the individual estimates and for a possible selection of showers with high-quality energy estimates. Another example is used for scaling image widths and lengths for *shape cuts* to those expected for gamma rays (either just scaling to mean 1.0, as used for HEGRA [40], or scaling and reducing to mean zero and variance 1.0, as used for H.E.S.S. [37]), again versus $R_c$ and $\log_{10}A$.

### 3.4. Gamma–hadron selection cuts

The traditional stereoscopic IACT analysis methods use both image shape and shower direction for discrimination between gamma-ray initiated showers and hadron showers. The former (*shape cuts*) are effective for point sources as well as extended sources but offer no useful discrimination against electron backgrounds. The latter (*direction cuts*) work with any kind of

background but are much more effective for point sources than for extended sources. Our baseline analysis here is optimized for point sources.

A key parameter for further analysis is the number of telescopes with cleaned images large and bright enough for further analysis and not too close to the camera edge, $N_{img}$, in the following simply *multiplicity*. The shape cuts use the width and length of each suitable image, after converting them to the corresponding *reduced scaled width* and *length* [37] (assuming an on-axis gamma-ray point-source for filling the look-up tables used for the conversion). In contrast to [37], the *mean* reduced scaled width and length of all $N_{img}$ suitable images in an event are not just (weighted) mean values but are re-scaled by predefined terms of the form $\sqrt{a + bN_{img}}$ to achieve a variance close to one (and a mean of zero), and thus efficiencies of fixed cuts are approximately independent of multiplicity $N_{img}$ and thus energy $E$. The actual cuts applied are energy-dependent, because high-energy hadron showers are easily rejected and larger cut efficiencies are possible at high energies. At low energies, more strict cuts will improve $Q = \epsilon_\gamma / \sqrt{\epsilon_p}$ (the quality factor for statistical errors) and $\epsilon_\gamma / \epsilon_p$ (for background systematics), with $\epsilon_\gamma$ ($\epsilon_p$) being the gamma-ray (proton) cut efficiency. Helium and heavy nuclei are much more effectively suppressed by shape cuts and are no longer a significant background after these cuts. Electron backgrounds cannot be suppressed by shape cuts.

The direction cuts for point sources are based on the multiplicity-dependent angular resolution, in the form of the 80% containment radius $r_{80}$ (to which an additional energy-dependent scaling factor can be applied but was not used, fixing this factor to 1.0). The resulting 80% cut efficiency is reasonable but is not optimal over the whole energy range. In the signal-limited high-energy regime it implies a (not necessary) loss of 20% of the signal, while at the background systematics limited low-energy end, a much tighter cut could improve signal/background by a modest amount.

Apart from the mandatory shape and direction cuts, there are optional cuts, based on the height of the shower maximum ($H_{max}$ cut, actually cutting on an energy-dependent range in the atmospheric depth of the maximum), on the energy reconstruction quality ($dE$ cut on the estimated error of the energy) and on the consistency of energy estimates from the individual images ($dE_2$ cut). The $dE$ cut takes into account that the energy resolution can be expected to improve with increasing energy because shower fluctuations get less relevant, the multiplicity increases and the average signal in individual telescopes with suitable images increases. Events failing the $dE$ cut are typically events with large core distances to the most nearby telescopes. Events with inconsistent energy estimates (failing the $dE_2$ cut) are typically those with bad reconstruction of the core position and those with a distribution of the Cherenkov light on ground being very different from the typical shape for gamma-ray showers.

The energy dependence of all adjustable cuts is parametrized as

$$c(E) = \begin{cases} c_1, & \text{for } E \leqslant E_1, \\ c_1 + (c_2 - c_1)\frac{\lg E - \lg E_1}{\lg E_2 - \lg E_1}, & \text{for } E_1 < E < E_2, \\ c_2, & \text{for } E \geqslant E_2. \end{cases} \quad (3)$$

Optimization of the relevant free parameters $c_1$, $c_2$, $E_1$, and $E_2$ was performed on an initial data set of the full configuration with 275 telescopes, for the given zenith angle, site altitude, NSB brightness (unless noted otherwise: 20°, 2000 m, dark sky, see Section 6 for details). No separate optimizations of these were undertaken for the sub-sets investigated, neither with the initial nor with the (much larger) corresponding final simulation data set.

Instead, as a final optimization, there is a choice between five pre-defined sets of image requirements (amplitude and number of pixels, dependent on the type of telescope because of different per-pixel NSB noise levels and different pixel scales). The pre-defined $h_{max}$, $dE$, and $dE_2$ cuts remain optional and are only applied when improving the sensitivity. The final free parameter is the minimum number of telescopes with suitable images. These three choices are done separately for each energy interval and each choice of observation time. The common picture emerging from this final optimization is:

- At the lowest energies, very loose cuts are required to get any signal at all; the low image quality as well as shower fluctuations result in both poor gamma–hadron discrimination and poor angular resolution. Due to the resulting high background, the sensitivity is typically limited by background systematics, at least for multi-hour observations and energies close to the detection threshold.
- At intermediate energies, enough telescopes acquire images of sufficient amplitude to apply strict image cuts, strict selection cuts, and high multiplicity. This is the region demanding most CPU time in simulations, since only a tiny fraction of the hadron showers passes all cuts.
- At the highest energies, the sensitivity is usually signal limited, and background does not play an important role. Using as much signal as possible, with loose cuts and low multiplicity, is of prime importance for best sensitivity.
- Optimal cuts for short observation times tend to be looser than for long observation times since background systematic uncertainty is less of a problem and signal limitation sets in at lower energies than for long exposures.

### 3.5. Significance of gamma-ray signals above backgrounds

For the significant detection of a gamma-ray point source the traditional requirements are a five standard deviation ('5-sigma') statistical significance ($S \geqslant 5$) and the presence of at least 10 excess events above background.

For calculating the statistical significance of a gamma-ray signal above some background, we use Eq. (17) of Li and Ma [43]. By convention we assume a signal-free background region five times larger than the signal region ($\alpha = 0.2$). The actual background region in which we register the – at high energies very few – simulated background events passing the cuts is independent from that. The registered (and known to be) signal as well as background events are weighted to correct for the different regions as well as for the different spectra in simulations and nature. The resulting signal and background in the source regions, with event weights and region corrections applied, are denoted as $N_\gamma$ and $N_{bg}$ in the following. In the Li and Ma notation, $N_{on} = N_\gamma + N_{bg}$ and $N_{off} = N_{bg}/\alpha$.

Due to possible systematics in background subtraction (resulting from zenith angle, position in the field of view, star light, broken pixels, or from a non-uniform distribution of PMT quantum efficiency or high voltage, etc.) we also require that the signal excess is at least five times the assumed background systematic uncertainty of 1% of the remaining background after cuts. Whether this level of 1% – better than what is currently achieved for example with H.E.S.S. [44] – can be reached, may depend on the technical implementation of the cameras as well as on calibration and monitoring procedures.

In the transition from statistics-limited to systematics-limited sensitivity, the baseline analysis as presented here combines the requirements such that, for example, a signal of six times the background systematic uncertainty and also six times the statistical fluctuation cannot result in a detection, despite (barely) fulfilling the individual requirements. Apart from this little detail, our requirements for the sensitivity limit for any given observation time (usually 50 h) can be summarized as

$S \geqslant 5$ (following [43] Eq. (17)),

$N_\gamma \geqslant 10$,

$N_\gamma/N_{bg} \geqslant 0.05$,                                    (4)

$\alpha = 0.2$.

For the differential sensitivity, we apply these requirements for each energy interval – typically with five intervals per decade of reconstructed energy, i.e. intervals of the decimal exponent of 0.2 (or 0.2 dex for short) – while for integral sensitivity they are applied just for the total signal and background. Integral sensitivity curves as a function of energy are a traditional means for describing detector performance in VHE gamma-ray astronomy, but are not used in this paper because they do not show the actual energy regime where an assumed power-law spectrum is most significant. Integral sensitivity also heavily depends on the assumed spectral index and care has to be taken to not extend it to energies below those where gamma rays can be readily detected, to avoid extrapolation with the assumed spectrum. Differential sensitivity does not suffer from these problems and is therefore preferred although it depends on the bin size and is not directly comparable with the integral sensitivity available for older experiments.

## 4. Alternative analysis methods

Independent parallel approaches for the improvement in CTA sensitivity have been successfully applied to the full CTA MC simulations and are presented in this section. The standard output of the CTA MC simulation can be processed with read_hess [22] and derived programs or it can be converted into other formats, either at the raw data (ADC counts) level or at the level of calibrated shower images (pixelwise charge and arrival time information). Among the alternate formats are several ROOT-based formats [45] which can be further processed for analysis with MARS[3] or HAP.[4] As shown in Section 8, these advanced analysis approaches achieve a sensitivity which is better by a factor of about two with respect to the Hillas-based analysis procedure as described in the preceding section.

All analysis methods presented here start by identifying the pixels with a significant signal with a procedure similar to that described in Section 3.1. The thresholds applied for the cleaning may vary depending on the analysis method.

### 4.1. IFAE analysis

In this analysis,[5] image cleaning and Hillas parameterization [39] proceed in a similar way to the standard analysis, but with somewhat looser criteria for inclusion of a pixel in an image (tail-cut levels of 3.0 and 6.0 p.e.), and some additional parameters, such as the fraction of the total light contained in the two brightest pixels (concentration) also calculated. The image amplitude is required to exceed 50 p.e. and the image centroid is required to be in the inner 80% of the radius of the field of view.

The shower axis direction and impact point on the ground are estimated by a minimization technique. Energy reconstruction makes use of look-up tables in a similar way to the baseline analysis, but with an additional dependence on the shower maximum. For background suppression this analysis makes use of the multivariate classification method known as Random Forest (RF), as used in the standard MAGIC analysis [47]. To exploit the information from all the telescopes triggered in a CTA event, one RF (containing 100 trees) for every type of telescope in the simulation is

built, using the image parameters as input variables (size, width, length, concentration) together with geometric quantities obtained from the stereoscopic reconstruction. The output of the RF is a single value in the range [0.:1.] for each image, which describes the hadronness of an event. The global event hadronness is found from the weighted average of the individual telescope values. Finally, for every bin in reconstructed energy, the cuts in (global) hadronness and in the squared angular distance from the reconstructed event direction to the nominal source position are scanned in a range of gamma-ray efficiency from 40% to 90%, to optimize the point-source flux sensitivity in each bin.

### 4.2. SAM analysis

The shower axis maximization (SAM) analysis differs from the baseline in that additional information is used for the reconstruction of the shower axis and in the methods used for background rejection [48]. The method begins with image cleaning and Hillas parameterization that are identical to the baseline approach. An iterative approach to find the best shower axis (a four-dimensional likelihood maximization) with look-up tables filled from MC gamma-ray simulations used to define the expected mean (and probability distribution) of image parameters for a given trial shower axis. This fit procedure [49] is performed using the following parameters: the orientation of the shower images in the camera (similar to standard reconstruction), the gradient of pixel trigger times in the shower image, the image centroid displacement from the trial shower origin and finally the consistency of energy estimates between telescopes. The event likelihood (goodness-of-fit) is used as an additional gamma/hadron separation parameter.

Once the event reconstruction has been completed, background rejection is performed by use of a neural network (NN), built using the ROOT TMVA [50] framework. A NN is created for each telescope type, using telescopewise parameters (including the goodness-of-fit), and all telescopes within a single event passed through their respective network. As for the IFAE analysis, the resulting event classification is a weighted average of classifications from all triggered telescopes. An energy-dependent cut is then made on this classifier, with the cut value being optimized to produce the highest differential sensitivity in each energy bin.

### 4.3. Paris-MVA analysis

In the Paris-MVA (multi-variate analysis) approach a 3D-model reconstruction [51] is coupled to a TMVA background rejection to achieve improved sensitivity at low energies as already demonstrated for H.E.S.S. [52] and then adapted to CTA [53]. Camera images are cleaned and parametrized as described for the baseline analysis (tail-cut levels 5.0 and 7.0 p.e.), with an initial direction estimated from the baseline shower-axis reconstruction. This initial shower axis is refined using the 3D-model reconstruction technique which models the Cherenkov photon emission in the atmosphere by a 3D-photosphere, assumed to have a Gaussian distribution along all axes. This model is used to predict the distribution of Cherenkov light in the cameras of a telescope array by adjusting the intrinsic parameters of the shower to achieve a good fit using a maximum-likelihood optimization of the ensemble of shower images. Energy reconstruction is performed in a similar way to the IFAE analysis but the method for the energy evaluation per telescope is somewhat different (see [52] for details).

Background discrimination is performed through an energy-binned multivariate procedure using Boosted Decision Trees (BDT) again implemented in the TMVA framework. The standard discriminant parameters used are the reduced-scaled Hillas width and length, the reduced 3D-width, its error, and the best-fit depth of shower maximum (3D-depth). Three new parameters have been

---

defined which identify incoherencies in the 3D-model shower fitted images with respect to the observed images. These additional parameters concern the angle between the reconstructed shower directions for the fitted versus observed images, the ratio of the energy estimates calculated for fitted versus observed images, and finally the deviations between measured image size and that expected from the look-up tables. Best-possible signal-to-noise ratio in each energy bin is obtained via a cut made on the BDT classifier output and an energy-dependent angular cut.

## 5. Interface to the physics working group

The physics working group has the goals of preparing the physics program of CTA, identifying key science programs, and defining benchmark physics targets and the required instrument performance for them. In order to explore the expected physics results for selected case studies and the impact of the instrument performance on the details of the physics output, simulations of physics cases using realistic CTA performances are required. To enable these detailed physics studies, the MC working group provides so-called "CTA performance files" in ROOT format, which describe the response of a given CTA layout. A set of tools is then provided to simulate specific physics cases, such as an energy spectrum of a source, a light curve, or a spatial morphology of the astrophysics phenomenon.

### 5.1. Performance files

The CTA performance files include histograms to describe in sufficient detail response functions of a given CTA layout, generally functions of the reconstructed energy (with five bins per decade) and of the offset angle with respect to the camera center. In particular, they include the point source differential sensitivity, the remaining background rate (for point sources as well as per square degree), the effective area (both as a function of reconstructed as well as of true energy), the angular resolution (68% and 80% containment), the energy resolution (r.m.s.), and also the two-dimensional energy migration matrix.

The response functions depend on the analysis chain used and optimization criteria applied. Also, the response functions depend on the altitude of the foreseen observatory, on the night sky background brightness, and on the zenith angle of the simulated observations.

### 5.2. Tools for simulations of the physics cases

Several tools have been created to enable a homogeneous comparison between specific physics cases and individual studies of the required performance. The tools include:

- Simulation of an energy spectrum of a user specified source at a user specified offset from the camera center. The simulated source might be a point like source or an extended source with various morphologies.
- Comparison between two simulated spectra. This tool aims for a solid statistical comparison between two physics scenarios in order to answer the question if CTA will be able to distinguish between them.
- A sky map tool to represent CTA response to extended sources of different morphologies and offsets from the camera center.

All tools have the same concept, which is described here. The user has to provide an energy spectrum of the source, spatial morphology and the observation time. The photon flux rate is calculated in bins of offset distance from the camera center and is folded with the corresponding effective collection area of the CTA array. The energy migration from true gamma-ray energy into the reconstructed energy is done according to the migration matrix, which is re-weighted depending on the spectral shape of the input distribution. The expected number of events in the signal region is calculated by summing up gamma rays from the simulated source and expected background level in a particular offset bin. Both signal and background event numbers are randomized according to Poisson statistics. The number of excess events and its error are calculated by assuming that the background level is estimated in a five times larger region than the signal region. The significance of the excess is calculated according to the prescription in [43]. Only bins that fulfill the following criteria are accepted:

- Significance of the excess in the bin is above 3.0 sigma.
- Number of excess events in the bin is 10 or more.
- The excess is larger than 3% of the background in the bin.

The resulting histograms (spectra, integral fluxes, sky maps) can be used for further analysis and are used to judge the power of a particular CTA array.

## 6. The production-1 configuration

The goal of the first CTA mass production of simulations was to characterize the performance of as many, and as varied, CTA candidate configurations as possible. Memory constraints on the computing nodes limited the simulation to a total of 275 telescopes, with only a small fraction of these telescopes being used in any given candidate array. Most simulations were made for an altitude of 2000 m (typical of several sites under consideration) and with an geomagnetic field strength and orientation intermediate between that found in southern Africa and the Canary Islands. NSB levels usually correspond to dark sky (a remote site like H.E.S.S. or MAGIC, no moon light, and a sky region off the Galactic Plane). Some simulations were also carried out for higher altitude sites (see Section 8.4) or for a brighter night sky (partial moon light, see Section 8.3). Most of the analysis work presented in this paper is based on simulations at 20° zenith angle, while simulation data are also available for 50° zenith angle. These simulations include billions of showers, each used multiple times at different impact positions, resulting in well over 100 billion events (mainly protons as the dominating background), with approximately one out of a 1000 events resulting in a stereo trigger of two telescopes or more.

Five different types of telescope were used in these simulations, three types with parameters close to those still under consideration for CTA, the large-, medium- and small-sized telescopes (LST, MST, SST) and are described in Table 1. Three telescope sizes are required to achieve the very large energy range of CTA in a cost-efficient way, with approximate trigger thresholds for the three components at 20 GeV, 100 GeV and 1 TeV. Davies–Cotton optics were used for the MST and SST telescope types and parabolic optics for the LSTs. The better off-axis performance of Davies–Cotton optics is important for the wider f.o.v. telescopes, whereas the negligible time-spread introduced by the parabolic optics is more important for the modest f.o.v. LST. These three telescope types share a common physical pixel size of 5 cm, the idea being to simplify the design and construction process through shared photosensors and other camera components. The angles subtended by the pixels in each of these telescope types are then close to the FWHM of gamma-ray images at the nominal threshold energy of each type. A field of view at the upper edge of the range under consideration was adopted for each telescope type, so that the full range could be studied by removing pixels from the analysis at a

**Table 1**
Geometrical parameters of the three main telescope types assumed in simulations.

| | Large (LST) | Medium (MST[a]) | Small (SST) |
|---|---|---|---|
| Diameter $D$ (m) | 24.0 | 12.3 | 7.4 |
| Dish shape[b] | Parab. | DC | DC |
| Mirror area (m$^2$) | 412 | 100 | 37 |
| Mirror tiles | 594 | 144 | 120 |
| Tile diam. (m) | 0.90 | 0.90 | 0.60 |
| Focal length $f$ (m) | 31.2 | 15.6 | 11.2 |
| $f/D$ | 1.30 | 1.27 | 1.51 |
| f.o.v. diam. (°) | 5 | 8 | 10 |
| Camera diam. (m) | 2.8 | 2.2 | 2.0 |
| No. of pixels | 2841 | 1765 | 1417 |
| Pixel diam. (°) | 0.09 | 0.18 | 0.25 |
| Pixel diam. (mm) | 49 (50[c]) | 49 (50[c]) | 49 (50[c]) |

*Notes*: The diameter, $D$, is defined by the outermost mirror edges while the effective diameter of a circle with the given mirror area would be smaller. The mirror area is corrected for inclination. Mirror tile and pixel diameters are flat-to-flat (all being hexagonal). The camera diameter is for the camera body used in ray-tracing.

[a] The MST-WF is a variant with the same mirror as an MST, except for $f = 16.8$ m, a $10°$ f.o.v. diameter and $0.25°$ pixels like an SST.

[b] Parabolic or Davies–Cotton (DC).

[c] Including a 1 mm gap between pixels.

later point. A wide f.o.v. version of the MSTs, denoted MST-WF, was considered as an alternative to SSTs, with MST-like dish but SST-like 0.25° pixels and 10° f.o.v. (see Table 1).

In terms of photosensors, the three main telescope types share hexagonal pixels with 50 mm spacing, with a bi-alkali type quantum efficiency of PMTs having a low afterpulsing ratio. Readout is assumed at 1.0 gigasamples per second (GS/s) with dual gain and 12-bit ADCs, similar to H.E.S.S. cameras, resulting in a dynamic range from 0.25 p.e. (electronic noise) to more than 5000 p.e. (saturation in the low-gain channel).

Fig. 5 shows the telescope layout chosen for these simulations. For the low-energy domain of the LSTs, effective collection area is less critical than a low trigger threshold and the best possible background rejection power. As a consequence, the LST component is made up of a small number of large (24 m) telescopes with moderate separations (less than the Cherenkov shoulder radius of $\sim$120 m at 2000 m altitude). The final layout incorporates 10 LSTs, allowing subsets of 2–6 telescope combinations to be selected with different spacings. Possible LST subsets include both squares and equilateral triangles of both 75 and 105 m side length.

The MST subarray provides most of the sensitivity in the core energy range of CTA (0.1–10 TeV) with $\sim$25 telescopes of 12-m class. For the MSTs the gamma-ray collection area is a critical factor, and the best trade-off between event-quantity (large area coverage) and event-quality (high-telescope-multiplicity events) is not obvious without detailed simulations. As a consequence, a wide range of spacings for the MST component were tested. The 275 telescope configuration incorporates regular grids of up to 45 telescopes with 60, 85, 120, 170, and 240 m spacings and a 25 telescope array with 340 m spacing, as well as a huge number of multi-baseline alternatives.

The SST telescopes are required to provide a multi-km$^2$ collection area above a few TeV. Possible solutions include $\sim$3 m telescopes of moderate ($<$150 m) spacing or more widely spaced larger telescopes. For classical photomultiplier tube (PMT) cameras and telescopes much smaller than 12 m, the camera cost dominates and very small telescopes are disfavored relative to widely spaced telescopes of larger size. The 7.4 m size adopted is close to optimal in terms of maximum area coverage at a fixed total array cost. The SST array is arranged around the MSTs, with grid-like and island-like layouts incorporated, with 180 m and 240 m spacings.

The candidate array layouts described in Table 2 were selected from the production-1 configuration with the goal of exploring a wide region of the phase space in terms of the balance of sensitivity across the CTA energy range and the trade-off between event quality and quantity. CTA South candidates were chosen to have a fixed nominal telescope construction cost of 80 M€ (in 2005 €) and to have significant sensitivity beyond 100 TeV. Northern array candidates NA and NB have half this nominal cost and no (or almost no) highest-energy component. Arrays E and I can be considered as base-line *balanced* layouts, in terms of the distribution of resources across the full CTA energy range. Arrays A, B, F and G are more focussed at low energies and C, D and H at high energies. NB is a higher energy focussed alternative to NA.

## 7. Performance of different layouts with the baseline analysis

### 7.1. Assumptions on source and background spectra

Simulations were set up to generate primary particles of power-law differential spectra following $E^{-2}$ (requiring about the same CPU time per decade in energy for the shower simulations) or even harder ($E^{-1.7}$, to get enough showers at the highest energies). All background particle spectra and most astrophysical gamma-ray source spectra are substantially softer than $E^{-2}$, and they may not even follow a power-law. Nevertheless, we assumed power-law spectra in the following, except for the electron (and positron) background (see Table 3). The latter was described by a log-normal peak of total flux $L$, median energy $E_p$ and width parameter $w$ on top of an $E^{-3.21}$ power-law spectrum, without any cut-off – largely consistent with measurements but rather conservative at TeV energies. Our assumed background spectra are based on measurements by BESS [54], Pamela [55], Fermi [56] and other experiments [57,58]. Gamma-ray source spectra are typically assumed to follow an $E^{-2.57}$ spectrum (as in the assumed Crab Units spectrum used as a sensitivity scale) but other spectra are possible. All results presented in this paper, unless noted otherwise, are based on this $E^{-2.57}$ assumption.

### 7.2. Point source sensitivity on-axis

The sensitivity of more than 50 different subset arrays extracted from the simulation data set with the 275 telescope configuration were evaluated in the way described in Section 3. Most of these arrays were selected to have an installation cost of 80 M€ in our cost model. These include arrays A–K for the main (southern) layout candidates, some compact, some more extended, some without LSTs, some without MSTs, and some without SSTs but most of them with three types of telescopes. Other subset arrays include several smaller northern site layout candidates (NA, NB) and a wide range of MST-only arrays with different separations and with different fields of view.

Image cleaning (adjusted to the different NSB levels in the different telescope types), five image selection rule sets ('extra-soft' to 'hard', with different requirements on image amplitude and number of pixels included), and the energy dependence of various shower-selection cut parameters were defined in advance. Integral and differential sensitivities were evaluated for each of the image selection rule sets, for each multiplicity of telescopes with useful images from two up to eight, and including or ignoring the optional $H_{max}$, $dE$, and $dE_2$ selection cuts, allowing for a final optimization as the last step.

Fig. 6 shows the on-axis point-source differential sensitivity of arrays A to K at 20° zenith angle. It can be seen that there are three categories: compact arrays (usually without small telescopes), extended arrays (without large telescopes), and *balanced arrays* which try to find a compromise between the compact and extended cases. At the lowest energies, the sensitivity curves split
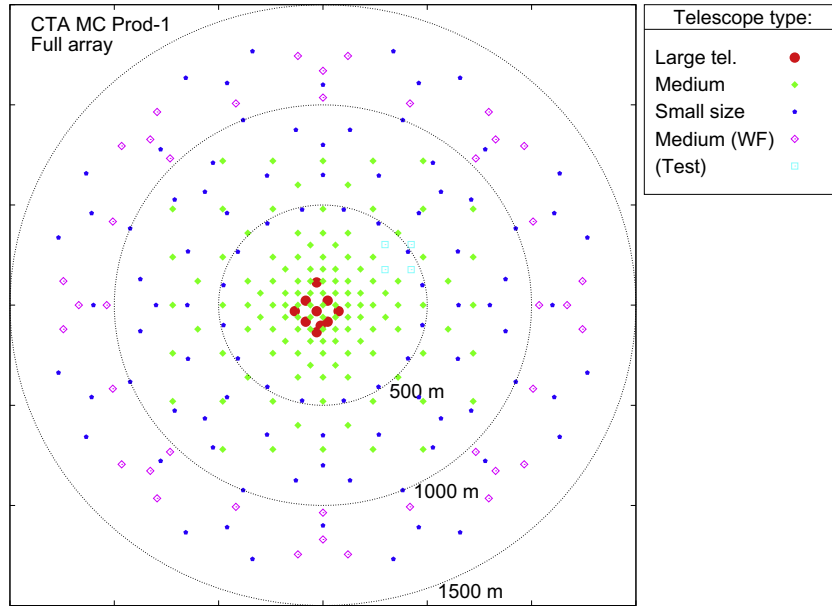
**Fig. 5.** The 275-telescope configuration used in the simulations described here, with LSTs shown in red, MSTs in green and SSTs in blue (see Table 1 for details), additional telescopes are shown in magenta and cyan. The dashed circles illustrate radii of 0.5, 1.0 and 1.5 km. (For interpretation of the references to color in this figure legend, the reader is referred to the web version of this article.)

**Table 2**
Candidate arrays for CTA South (A–K) and CTA North (NA, NB). For each telescope size the number of telescopes of that size is given, together with the field of view used in the analysis.

|    | LST | MST | SST |
|----|-----|-----|-----|
| A  | 3 (5°) | 41 (8°) | – |
| B  | 5 (5°) | 37 (8°) | – |
| C  | – | 29 (8°) | 26 (10°)[a] |
| D  | – | 41 (7.4°) | 16 (10°)[a] |
| E  | 4 (4.6°) | 23 (8°) | 32 (10°) |
| F  | 6 (4.8°) | 29 (6.3°) | – |
| G  | 6 (5°) | 9 (8°) | 16 (10°) |
| H  | – | 25 (7°) | 48 (10°) |
| I  | 3 (4.9°) | 18 (8°) | 56 (9°) |
| J  | 3 (4.9°) | 30 (8°) | 16 (9°)[a] |
| K  | 5 (5°) | – | 72 (9.5°) |
| NA | 4 (5°) | 17 (6°) | – |
| NB | 3 (5°) | 17 (6°) | 8 (8°) |

[a] With wide-field versions of MSTs instead of actual SSTs.

**Table 3**
Spectral parameters of assumed signal and background differential spectra.

| Primary particle type | Norm.[a] $N$ | Spectral index $k$ | Log-n. ampl.[a] $L$ | Location [TeV] $E_p$ | Scale $w$ |
|----|----|----|----|----|----|
| $\gamma$ | Var.[b] | −2.57 | | | |
| p | 0.096 | −2.70 | | | |
| He | 0.0719 | −2.64 | | | |
| N (CNO) | 0.0321 | −2.67 | | | |
| Si (heavy) | 0.0284 | −2.66 | | | |
| Fe | 0.0134 | −2.63 | | | |
| $e^-$ (and $e^+$) | $6.85 \times 10^{-5}$ | −3.21 | $3.19 \times 10^{-3}$ | 0.107 | 0.776 |

$dF(E)/dE = N \times (E/1\,\mathrm{TeV})^{-k} + L/(Ew\sqrt{2\pi})\exp(-(\ln(E/E_p))^2/2w^2)$ (see text for more details on log-normal component).

[a] $[1/(\mathrm{m}^2\,\mathrm{s}\,\mathrm{sr}\,\mathrm{TeV})]$.

[b] Gamma-ray sources in $[1/(\mathrm{m}^2\,\mathrm{s}\,\mathrm{TeV}]$ or C.U. (Crab Units): 1 C.U. $= 2.79 \cdot 10^{-7}\,\mathrm{m}^{-2}\,\mathrm{s}^{-1}\,\mathrm{TeV}^{-1} \times (E/\mathrm{TeV})^{-2.57}$.

up by the number of large telescopes (5, 4, 3, or none). At the highest energies, the sensitivity is always signal limited and thus dominated by the area covered.

Statistical errors on the derived sensitivity (mainly from the finite number of proton showers passing cuts) are neither included in Fig. 6 nor the following since they are highly correlated between different array layouts (sharing the same simulated showers and also part of the telescope data). Statistical errors are actually smaller than the fluctuations seen from energy bin to energy bin, which also result from the optimization process (e.g. integer values of multiplicity).

Good examples of balanced arrays can be seen with arrays E and I. Array E, with four large telescopes, performs slightly better at low energies than array I, with only three large telescopes. At large energies, array I with its extended set of small telescopes outperforms array E by typically a factor of 1.5. Array B is a typical case for a compact layout while array D is one of the extended layouts without any large telescopes (see Fig. 7).

The candidate layouts for a northern CTA site, without extended sets of small telescopes and with fewer mid-size telescopes, are rather similar in their performance to the compact full layouts but with slightly inferior sensitivity at a TeV and above.

The different limiting factors for the sensitivity – signal, statistics, or background systematics – also result in different dependence of the sensitivity on observation times $T$: proportional to $1/T$ at the highest energies, $\propto 1/\sqrt{T}$ at intermediate energies, and substantially weaker than $1/\sqrt{T}$ at the lowest energies (see Fig. 8). Note that the final optimization of image selection, multiplicity, and choice of optional cuts has been done separately for each observation time, typically resulting in looser selections for shorter observation times. Fig. 8 also demonstrates that array I is in fact a well-balanced array, with little sensitivity loss against specialized arrays in any energy range.

The contribution of the different types of telescopes to the overall sensitivity for on-axis point sources is demonstrated for array I in Fig. 9, for an observation time of 50 h. The cross-over between LSTs and MSTs is seen at about 250 GeV, that between MSTs and SSTs at about 4 TeV. At these cross-over points, the larger telescopes contribute fewer but higher quality data while the smaller telescopes provide a larger effective area but with lower image quality. At both transition points, the combined sensitivity is
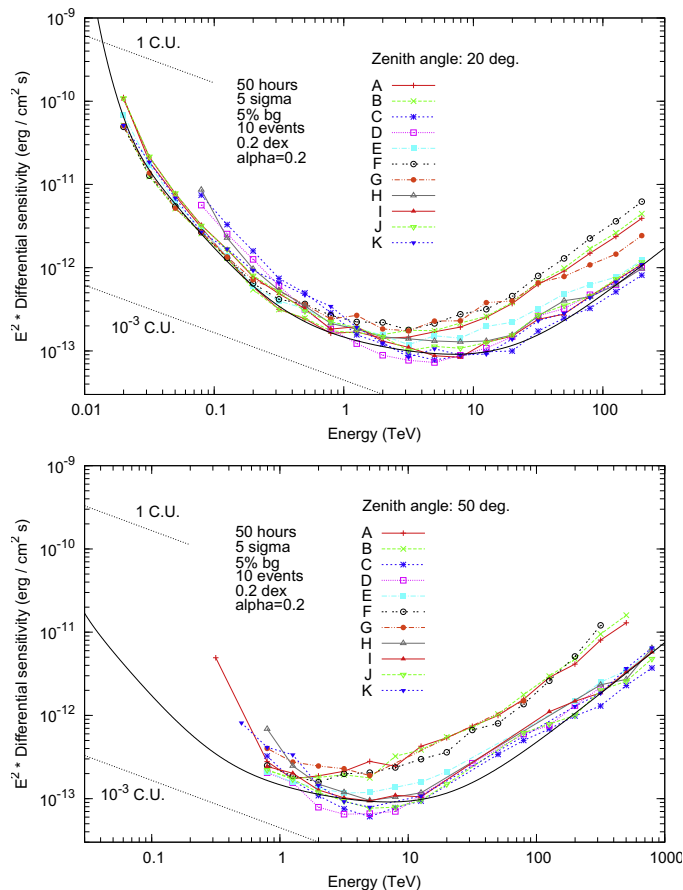
**Fig. 6.** Point source sensitivity of 11 CTA candidate array layouts (of identical estimated costs, for CTA South) for 50 h observation time, evaluated with the baseline analysis method. Note that this differential sensitivity corresponds to an independent detection in each energy interval and is much more strict than the conventional integral sensitivity – but almost independent of the assumed spectrum. The solid black line is an approximation of the best performance of any of these arrays at any energy (except *D* which is highly specialized for energies of a few TeV), for 20° zenith angle. The Crab Unit (C.U.) and milli-C.U. fluxes as used in this paper are indicated for comparison. Top: 20° zenith angle, bottom: 50° zenith angle.

almost a factor of two better than that of the individual components. Near 1 TeV, though, the onset of low-quality SST data, with large effective area but poor gamma–hadron rejection deteriorates the combined sensitivity in our simple analysis method basically to the sensitivity of the MST data alone.

Because no small telescopes were assumed in the inner region of array I, the MSTs continue to contribute to the combined sensitivity up to the highest energies, despite possible signal saturation. At a smaller (10–15%) level, the presence of MSTs even improves the sensitivity at the lowest energies – where the MSTs are not expected to be triggered at all by gamma rays or electrons but still can reject some hadron background. Such background includes muons seen by MSTs or events where the LSTs only registered a small gamma-like sub-shower of a larger hadron shower.

The effect of a signal limitation at 1000 p.e. per pixel is also indicated in Fig. 9 by the thin lines with small symbols. Even though LSTs above several TeV and MSTs above a few 10s of TeV suffer from pixel saturation, with an impact on angular and energy resolution (see Section 7.3), this only happens in a regime where the sensitivity is signal limited and does not depend on angular resolution.

Finally, Fig. 9 also illustrates the relevance of the electron background on the combined sensitivity. This background is most relevant in the region of the 'shoulder' in the cosmic ray electron (and positron) spectrum at a few 100 GeV. Below about 200 GeV, the

rejection of proton-induced showers deteriorates substantially and the background is dominated by the protons. Above a few TeV, both the electron and the hadron backgrounds are at a very low level and the point source sensitivity is signal limited.

The second CTA site, in the northern hemisphere, is foreseen to be instrumented similar to array I excluding its extended SST component. As such, a northern CTA site could perform similar to the main site at low energies (unless affected by the geomagnetic field) to a few TeV. At energies above a few TeV, such a northern site will suffer from its much lower effective area.

### 7.3. Angular resolution and energy resolution

Angular and energy resolution in an installation with different instrument types (and separations between instruments increasing outwards) combine in ways which are not always intuitive. In a homogeneous array, increasing energy will result in more usable telescopes with, on average, improved data quality and therefore improving angular and energy resolution, at least to the point where the instruments start running into pixel saturation.

In a realistic array, showers of increasing energy will trigger smaller instruments in wider separations to their next neighbors. Most of its effective area may be from showers recorded with few and widely separated telescopes. A subset of the showers, typically those with shower cores closer to the array center, will be recorded with higher telescope multiplicity and data quality, providing a subset of high angular resolution and/or of high energy resolution. Figs. 10 and 11 show only the angular resolution and energy resolution achieved with cuts separately optimizing these resolutions, at minimum multiplicities between two and six.

### 7.4. MST inter-telescope separation and field of view

One important question related to the CTA layout is the correlation between optimum inter-telescope separation and the f.o.v. of a telescope. The available data allowed to study this with MST-only arrays of similar cost estimates. We extracted data for arrays of telescopes at a spacing of either 60 m, 85 m, 120 m, 170 m, or 240 m. At each of these spacings we used arrays of 37 telescopes with a f.o.v. diameter of 5.0°, of 32 telescopes of 6.0°, 27 telescopes of 7.0°, as well as 24 telescopes of 8.0°. Fig. 12 shows the resulting on-axis differential point-source sensitivity for 120 m separation. Except at the highest energies, a f.o.v. of only 5° is typically best – but the performance of fewer telescopes with larger f.o.v. is quite similar. For extended sources or when multiple sources can be studied at the same time – the typical case along the Galactic Plane – the larger f.o.v. comes with additional benefits. For this reason, the MST telescopes for CTA are foreseen to have cameras with a f.o.v. between 6° and 8°.

In Fig. 13 we have 7.0° f.o.v. cameras in 27 telescopes at different separations. It is obvious that separations below 120 m have no advantages at any energies, except at the very threshold. At energies beyond a TeV, the larger effective areas resulting from larger separations more than compensate for the poor sampling of each shower (seen in fewer telescopes). Since there is no separation that can optimize the performance simultaneously at all energies, a *graded layout* with inter-telescope separations increasing from the array center outwards will result in a better overall performance than a regular grid. Note that at larger zenith angles the Cherenkov light pool on the ground will increase and optimum spacings are always larger than at small zenith angles.

## 8. Comparisons for candidate array I with alternative analyses

We discuss the expected performance of the candidate array I that is obtained by using the alternative analyses described in
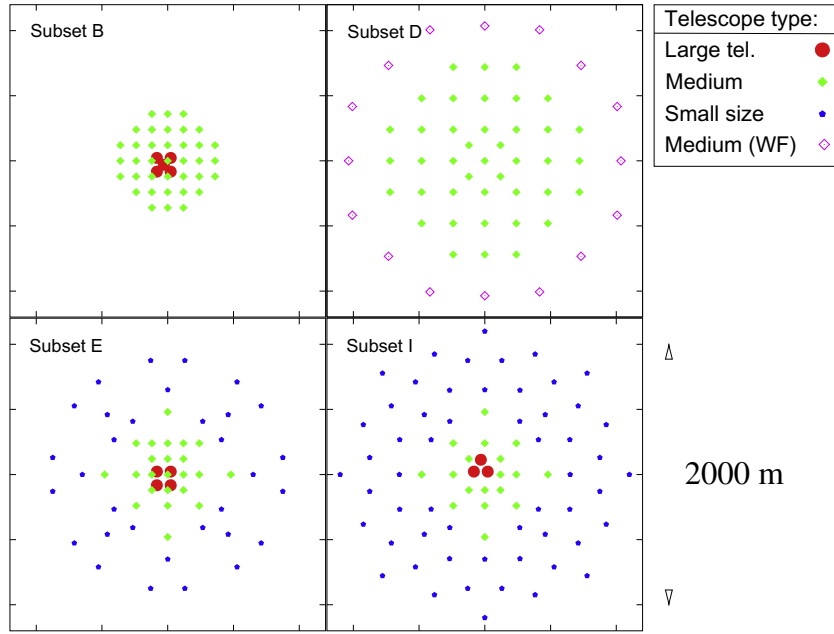
**Fig. 7.** Layout examples for a compact array layout (B), an extended layout without LSTs (D), as well as two balanced layouts (E and I).
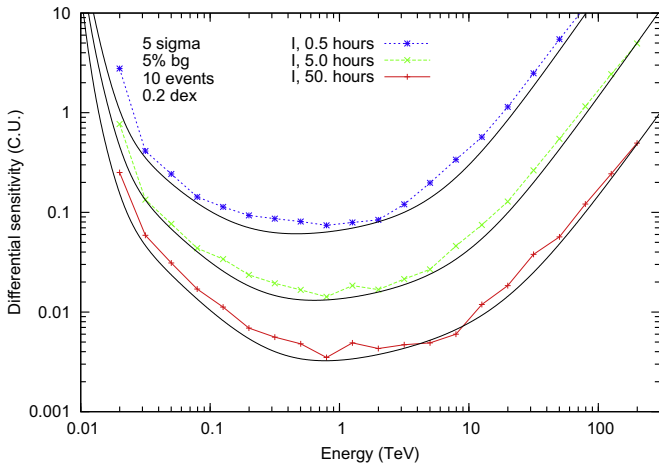


**Fig. 8.** Point source sensitivity of array I (in units of 1 C.U. $= 2.79 \times 10^{-7} (E/\text{TeV})^{-2.57} \text{ m}^{-2} \text{ s}^{-1} \text{ TeV}^{-1}$) for observation times of 0.5 h, 5 h, and 50 h, respectively. Also shown as black solid lines are approximations to the best performance of any of the 11 CTA South arrays at any energy (as in Fig. 6), for the given observation times. Array I, being close to this optimum at all energies, is indeed a well-balanced array.
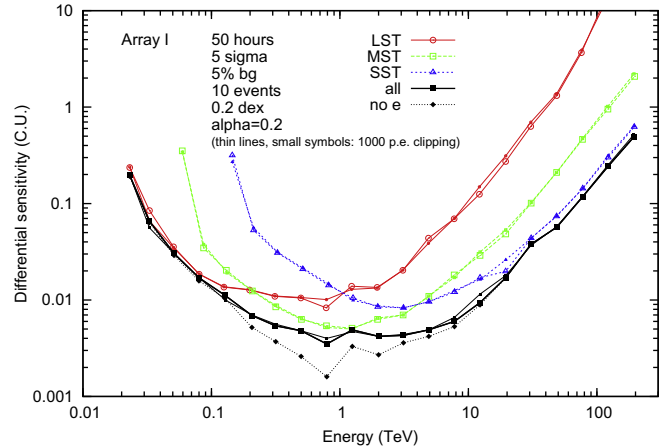
**Fig. 9.** Point source sensitivity of array I (solid black line, filled squares) and its components, 3 LSTs (red, open circles), 18 MSTs (green, open squares), 56 SSTs (blue, open triangles). Thin lines with small symbols illustrate the limited impact of a reduced dynamic range of PMT readout electronics. For the relevance of the electron background on the combined sensitivity see also the dashed black line with diamonds, where this background is ignored. (For interpretation of the references to color in this figure legend, the reader is referred to the web version of this article.)

Section 4. The array consists of 3 LSTs with a field of view (f.o.v.) diameter of 4.9°, 18 MSTs with a f.o.v. diameter of 8° and 56 SSTs with a f.o.v. diameter of 9°, whose positions on the ground are shown in Fig. 7. We also mention briefly comparisons between different site altitudes and for observations under partial moon light.

### 8.1. The differential flux sensitivity

The minimum detectable flux is determined, by demanding a minimum 5σ detection (using Eq. (17) from Li and Ma [43]), at least 10 gamma-ray events, and a gamma-ray excess of at least 5% of the residual cosmic-ray background. The differential flux sensitivities achieved from the alternative analyses are shown in Fig. 14, using five bins per decade in energy. Differences between sensitivity curves may be understood in terms of the respective

effective areas and residual cosmic-ray background rates, which are shown in Figs. 15 and 16, respectively. These effective areas and background rates are in turn dependent on the specifics of each analysis (see Sections 3 and 4 for details). This may include the image cleaning, quality cuts, shower reconstruction, and cosmic-ray background rejection power, along with the gamma-ray selection-cut optimization scheme that is employed for each analysis. The optimization is on sensitivity and good sensitivity can be achieved either with large effective area or low background. Therefore small fluctuations in simulated data can result in large apparent fluctuations in Figs. 15 and 16. The most sensitive analyses (SAM and Paris-MVA) approach levels of 2 milli-C.U. in differential sensitivity per bin at energies of around 1 TeV, or about 1 milli-Crab in integral sensitivity.
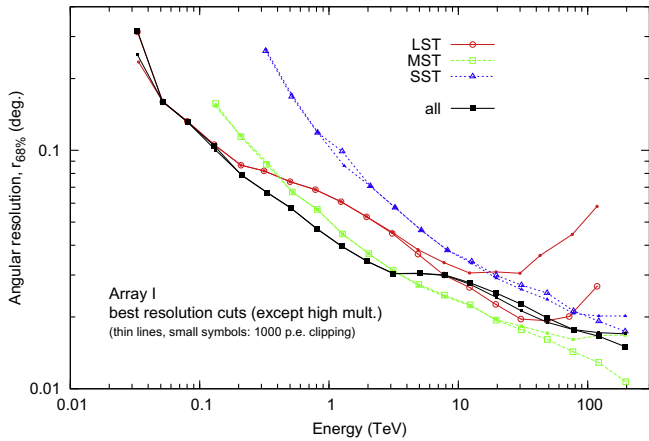
**Fig. 10.** Angular resolution of array I (68% containment radius) as a function of energy (lines and symbols as in Fig. 9). Cuts were optimized for angular resolution, at a minimum multiplicity between two and six. At energies above 5 TeV a pixel dynamic range limited to 1000 p.e. would have substantial impact on the LST angular resolution but basically no impact on the resolution of the full array. While the angular resolution of all telescopes is always better than that of the component dominating the effective area at a given energy, selecting data from a single component may improve angular resolution at the cost of a much reduced effective area.
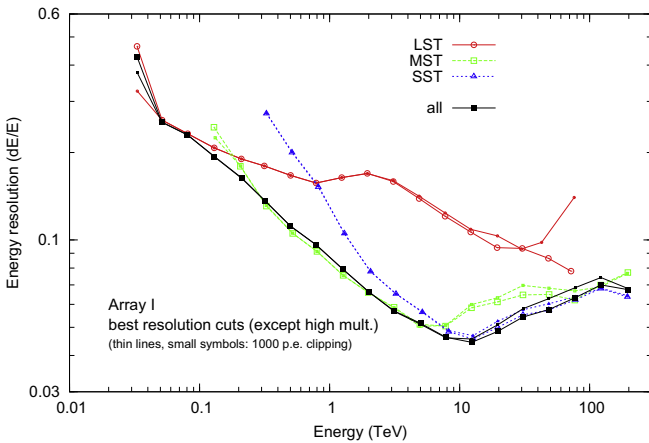


**Fig. 11.** Relative r.m.s. energy resolution $\sigma(E)/E$ of array I as a function of energy (lines and symbols as in Fig. 9). Cuts were optimized for energy resolution, at a minimum multiplicity between two and six.
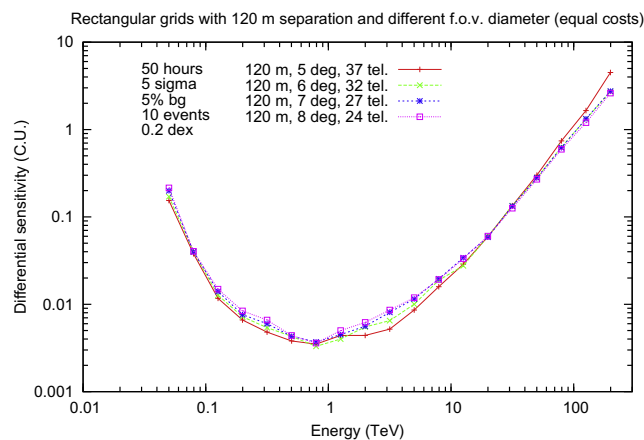


**Fig. 12.** Differential point-source sensitivity on-axis in C.U. for MST arrays of similar cost but with cameras of different f.o.v. (fewer telescopes for larger f.o.v., see text for details), for a 120 m inter-telescope separation and 20° zenith angle.
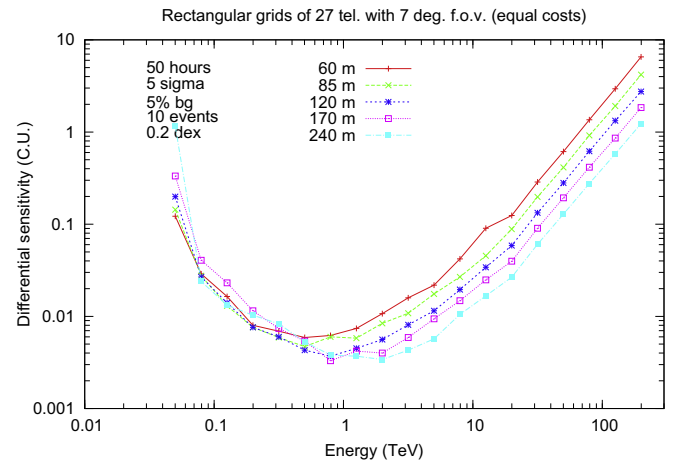


**Fig. 13.** Differential point-source sensitivity on-axis in C.U. for MST arrays of 27 telescopes with 7° f.o.v., at different inter-telescope separations (zenith angle: 20°).

In the range of 30 GeV to 3 TeV, the Paris-MVA analysis improves on the sensitivity of the baseline analysis, by up to a factor of 3.5. We note that the Paris-MVA analysis generally maintains a large effective area with respect to the baseline analysis, although it also yields the largest cosmic-ray background rate for energies above 300 GeV. The SAM analysis provides the best performance at multi-TeV energies, improving on baseline result by factors as large as 2.0, with effective areas not quite as large as Paris-MVA but compensated by low background rates.

### 8.2. The angular and energy resolutions

The gamma-ray events used to determine the angular and energy resolutions are those that pass the cosmic-ray background rejection cuts, which are used to obtain the respective differential sensitivity curves in Fig. 14. The $r68$ angular resolution, is defined as the angular radius from a point-like source that contains 68% of the events. This is shown as a function of the estimated energy for the case of candidate array I in Fig. 17. It varies, depending on the
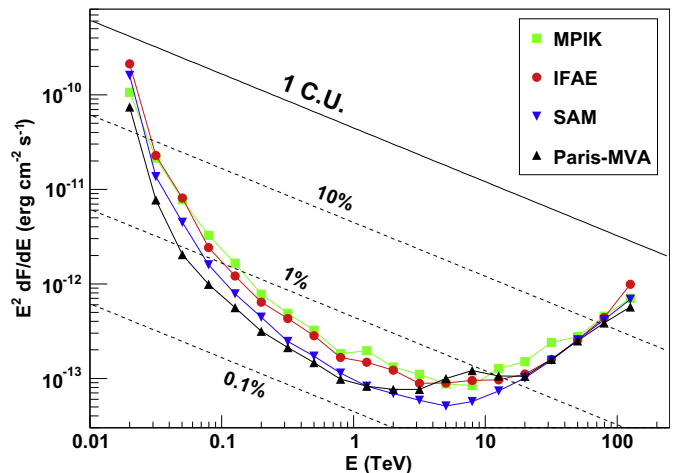


**Fig. 14.** Differential flux sensitivity of candidate array I given as a function of the estimated energy, for the baseline/MPIK (green squares), IFAE (red circles), SAM (blue triangles) and Paris-MVA (black triangles) analyses. The Crab Unit (C.U.) flux (solid black line) is shown for comparison, together with its 10%, 1% and 0.1% flux levels (black dashed lines). The differential sensitivities are optimized for an observation time of 50 h. (For interpretation of the references to color in this figure legend, the reader is referred to the web version of this article.)

analysis, from 0.2–0.5° at ∼20 GeV to 0.02–0.03° at ∼125 TeV. The different shower direction reconstruction methods and various cosmic-ray background rejection cuts lead to the noticeable spread in $r68$ values below ∼1 TeV between the alternative analyses.

A similar argument may be used to explain the differences between the alternative energy resolutions of the candidate array I, although here the methods used to determine the estimated energy also differ, as detailed in Section 4. We define the term 'energy resolution' to be the r.m.s. of the distribution $E_{est}/E_{true}$, where $E_{est}$ is the estimated energy and $E_{true}$ is the true energy. Fig. 18 shows the energy resolutions as functions of the estimated energy. The energy resolutions range between 0.3 and 0.50 at around 20 GeV to ∼0.05 at around 8 TeV. The poor energy resolution of Paris-MVA at high energies is being worked on.

### 8.3. Observations under partial moon light

The standard observing conditions of ground-based Cherenkov telescopes correspond to clear sky, with both Sun and Moon below the horizon, and lead typically to an average of 1650 h/yr of possible dark observation time. Allowing observations under moderate moon light conditions increases the total observation time by up to 30%. This can be of crucial importance in case of transient phenomena, such as flares of AGNs, phase-related activities as for binary systems, or GRBs. The MAGIC and VERITAS experiments both routinely perform observations under moon light conditions. MC simulations with a NSB 4.5 times higher to the one commonly in use have been performed. This corresponds to nights with the Moon above the horizon, approximately illuminated at 60%, although often moon-time observations can be carried out at less enhanced NSB. Trigger thresholds have been adjusted to obtain manageable trigger rates – while in reality also the PMT gain may get adjusted to reduce additional PMT aging. The simulations have been processed through the entire analysis chain, as discussed in the preceding sections, with somehow different cuts, particularly in the image cleaning steps to account for the higher NSB noise levels.

The final results are similar to those obtained for dark sky conditions [59], and hardly affect the performances above 1 TeV. Indeed, as expected, the moon light observing conditions mainly affect the low part of CTA energy range. In this part, due to higher
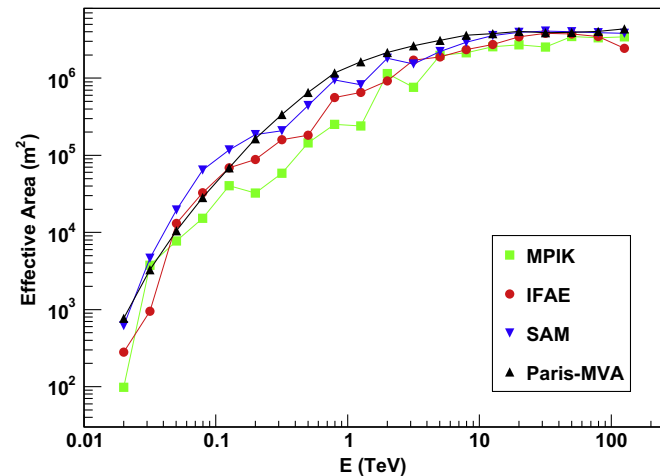


**Fig. 16.** Residual cosmic-ray background rate of candidate array I, given as a function of the estimated energy for the baseline/MPIK (green squares), IFAE (red circles), SAM (blue triangles) and Paris-MVA (black triangles) analyses. The differential sensitivities are optimized for an observation time of 50 h. (For interpretation of the references to color in this figure legend, the reader is referred to the web version of this article.)
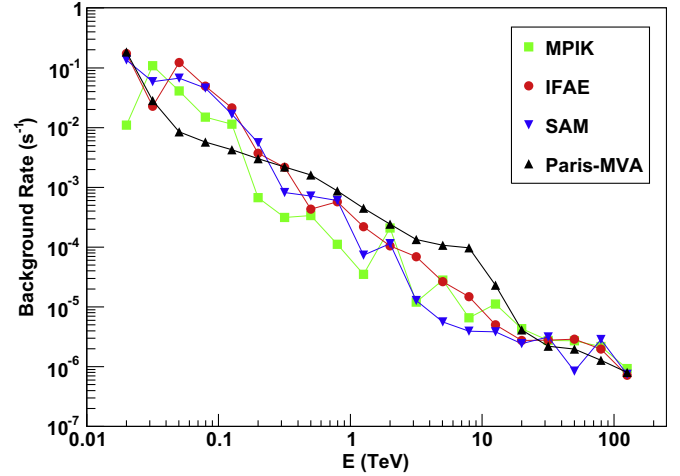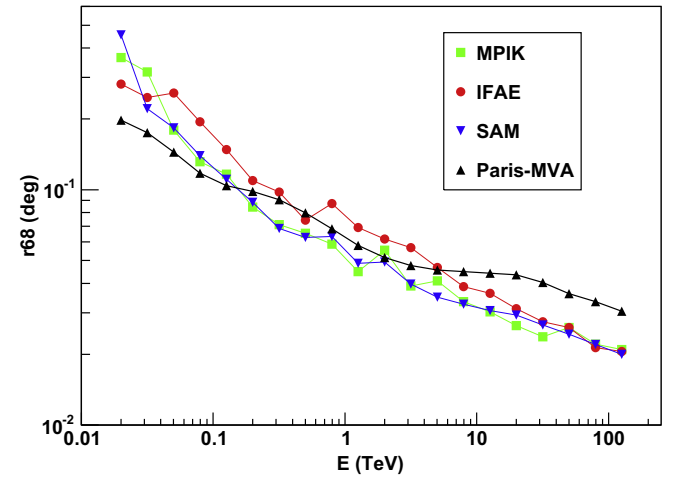


**Fig. 17.** Angular resolution (radius of 68% event containment, $r68$) of candidate array I, given as a function of the estimated energy for the baseline/MPIK (green squares), IFAE (red circles), SAM (blue triangles) and Paris-MVA (black triangles) analyses. The differential sensitivities are optimized for an observation time of 50 h. (For interpretation of the references to color in this figure legend, the reader is referred to the web version of this article.)

noise levels, and depending on the array layout, the energy thresholds are generally a factor of two higher and the sensitivities might be 10 times worse. However, in the core of CTA energy range around 1 TeV, not only the sensitivity but also the angular and energy resolutions are quite compatible with the results of dark sky observations.

### 8.4. High-altitude sites

The altitude of 2000 m has been assumed for most of the CTA simulations but the possible performance advantages (and disadvantages) of high-altitude sites have been investigated as well. First comparisons were carried out with arrays of 9 large telescopes at 2000, 3500, and 5000 m altitude [18,7]. High-altitude sites result in lower energy thresholds, mainly because the Cherenkov light gets less diluted when reaching ground. For the same
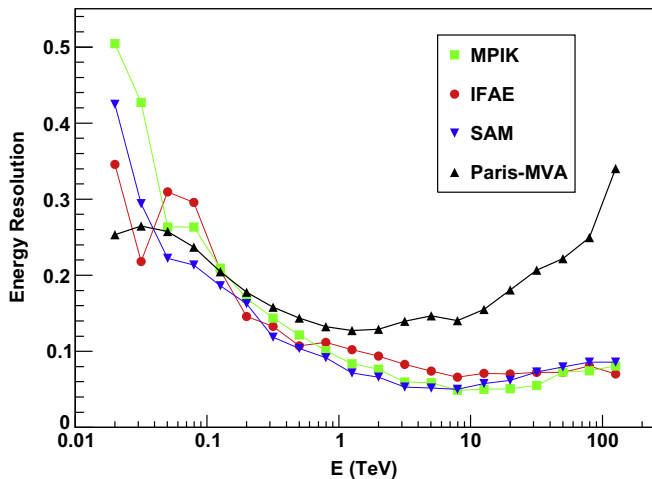


**Fig. 15.** Effective area of candidate array I, given as a function of the estimated energy for the baseline/MPIK (green squares), IFAE (red circles), SAM (blue triangles) and Paris-MVA (black triangles) analyses. The differential sensitivities are optimized for an observation time of 50 h. (For interpretation of the references to color in this figure legend, the reader is referred to the web version of this article.)

**Fig. 18.** Energy resolution of candidate array I, defined as the r.m.s. of the distribution of $E_{est}/E_{true}$, using the baseline/MPIK (green squares), IFAE (red circles), SAM (blue triangles) and Paris-MVA (black triangles) analyses. $E_{est}$ is the estimated energy, while $E_{true}$ is the true energy. The energy resolution is given as a function of the estimated energy. The differential sensitivities are optimized for an observation time of 50 h. (For interpretation of the references to color in this figure legend, the reader is referred to the web version of this article.)

reason, smaller telescope separations are needed, resulting in lower effective areas at medium to high energies. Images are also seen at larger distances from the shower direction, which may require a larger camera f.o.v. At the 5000 m altitude, gamma–hadron separation was found to suffer from too many Cherenkov-emitting particles in gamma-ray showers reaching ground level, resulting in more irregular gamma-ray images.

For the latter reason, as well as due to technological and cost implications of a high-altitude site, more detailed simulations of high-altitude sites were limited to 3700 m, for the same telescope configuration as in production-1. Neither were telescope separations optimized for the higher altitude nor were cost implications included in the array selection, e.g. using array I as for 2000 m. Initial results of different studies show that the energy threshold achieved at 3700 m is in general lower by 0.2 dex or more, and in the low energy domain ($E < 100$ GeV), the differential sensitivity achieved is generally at least a factor two better. At higher energies, the achieved differential sensitivities of the different layouts envisaged for CTA at high altitude are compatible with those obtained at 2000 m, perhaps marginally worse. However, the energy resolution generally degrades above a few TeV. Before firm conclusions can be drawn on an optimum site altitude, separate optimizations of telescope spacings at the different altitudes are required and cost implications (in telescope design, construction, and operation) should be represented in the array selection, for a performance comparison at fixed cost.

## 9. Future directions and hardware

### 9.1. Hardware improvements

The Monte Carlo simulation of the detector was done assuming a very preliminary design of the CTA telescopes. Both due to the hardware development and the feedback from the simulations, some of the designs being under discussion currently differ from the simulated one. Monte Carlo simulations are going onto understand the improvements and limitations of those modifications.

### 9.1.1. Changes in optical design

The initial simulations assumed a parabolic dish shape for the LSTs and a Davies–Cotton shape for MSTs and SSTs. While the par-

abolic shape has the advantage of negligible time-spread introduced by the optics, the classical Davies–Cotton design has the advantage of a better PSF at large off-axis angles. While the optics time-spread of SSTs is always small compared to the shower-intrinsic spread as well as the PMT transit-time jitter, the time-spread of Davies–Cotton MSTs is already dominated by the optics.

The MST optics has thus been redesigned and changed to an intermediate shape, with spherical dish of radius of curvature $R_c = 1.2f$. Note that Davies–Cotton has $R_c = f$ while a parabolic dish has a central radius of curvature of $R_c = 2f$. The modified MST optics is still close to a Davies–Cotton but with a significantly reduced time spread (0.7 ns r.m.s. instead of 1.0 ns). The slightly worse off-axis PSF of the intermediate shape is compensated by a small increase in its focal length (from 15.6 to 16.0 m).

A similar intermediate shape, but closer to parabolic, has also been recommended for the LSTs. Only muon rings, easily recognizable in images, have an intrinsic time spread short enough that they could take any advantage of the low time spread of a parabolic dish. Otherwise, both for gamma-ray showers and background, the intrinsic time spread of photons imaged into the same pixel has an r.m.s. value of the order of 0.5–1.0 ns in the energy and core distance range relevant for LSTs. The PMT transit time jitter (or spread) is of a similar magnitude. Considering that, an intermediate dish shape with an optical r.m.s. time spread of 0.6 ns has been recommended, which is closer to parabolic than Davies–Cotton but already offers improvements in off-axis PSF.

### 9.1.2. Camera trigger

The results presented in the previous sections all used a majority trigger logic with a low combinatorial factor, requiring that a pixel plus a number of its direct neighbors must have fired within a given gate width. None of the current hardware developments in CTA is focusing on such an algorithm yet, although some of the developed options are flexible enough to program it.

There are several trigger designs considered that use the analog signal from the PMTs and others that use digitized signals, either fully digitized samples (from FADCs) or comprising only one or two bits (from fast comparators).

- **Majority trigger:** The analog signal coming from each pixel is compared to an adjustable threshold (by a discriminator or comparator) and then the sum of discriminator/comparator outputs in a region (either analog or digital sum, basically the number of pixels above threshold at the same time) has to exceed an adjustable multiplicity value to result in camera triggers.
- **Analog sum trigger:** The analog signals from all pixels in a region are added and then compared to a minimum value to produce the camera trigger. Before adding the individual pixel signal, they can be clipped, limiting their maximum value and thus reducing the impact of afterpulses.
- **Binary trigger:** The analog signal from the photosensors is passed through a comparator at regular time intervals, essentially transforming the camera image to a binary pattern. With modern fast and flexible front-end electronics, complex trigger classification algorithms can be run on-line, processing the binary pattern in space and time. With additional thresholds, this trigger concept can emulate image cleaning algorithms, similar to those used for off-line image analysis.
- **Digital trigger:** The signal coming from the photosensors is continuously digitized by a FADC and the digital signal is used to take the trigger decision – which could be either a digital sum trigger with optional clipping or a digital majority trigger (or a mix of both), depending on the algorithms programmed into FPGAs. This scheme avoids front-end electronics like discriminators and comparators, but is currently only cost-effective for FADC sampling rates up to about 250 MHz.

Trigger simulation tools exist for all of these different schemes. The key quantities for assessment of any improvement of the trigger performance should be sensitivity, angular resolution, and energy resolution. The triggered images still need to be subjected to a reconstruction, and it is useless to trigger more images if that cannot help to better reconstruct the shower and to improve the gamma–hadron separation. Data analysis techniques are still improving and there might eventually be methods to recover some fraction of the events currently discarded – but at least with current analysis techniques the events barely triggered tend to have too low amplitude signals to be usable for reconstruction. The study of the impact of improved trigger schemes in terms of source sensitivity etc. is work in progress.

### 9.2. Optimal pixel integration time window

Most of the detected Cherenkov photons are emitted near the shower maximum and arrive at an IACT pixel within only a few nanoseconds time spread. As a consequence of the short time scale of Cherenkov light flashes, there is an optimum integration time which minimizes the error in collected pixel signal charge over NSB fluctuations. For short integration times, the Cherenkov signal should dominate over NSB. As the integration time increases, the shower fluctuations are smoothed out and the relative error on the integrated charge decreases. Once the bulk of the signal is integrated, a further increase of the integration time will degrade the accuracy due to the NSB fluctuations (see Fig. 19 (left)).

Even at high energies, most of the Cherenkov light can be collected within a ∼15–20 ns *per pixel* time window, see Figs. 19 and 20. The dynamic range of the pixel charges in the event shown in Fig. 20 is up to ∼$10^4$ p.e. As in most gamma-ray shower images, the largest signal amplitudes correspond to the shower maximum. The correlation between the optimal integration time and the signal amplitude in a pixel is clearly visible. A dynamic integration window, i.e. the one where the duration is varied as a function of signal amplitude to provide the best pixel charge resolution, could be an improvement with respect to a fixed duration integration time (see Fig. 19 (right)). Under conditions of dark sky the overall improvements are very small, since Poisson fluctuations dominate, but under partial moon light conditions more significant improvements can be envisaged. Whether the additional effort (and cost) of its technical implementation and calibration is worth this effort needs to be studied.

### 9.3. Readout strategy

As it has been mentioned, Cherenkov photons do not all reach a telescope at the same time. For instance, the time spread for photons coming from a 10 TeV shower can be, in extreme cases, as large as 200 ns while in a single pixel is at least one order of magnitude smaller. Actually, pixels receiving Cherenkov light only from a single particle may see all photons arriving within a fraction of a nanosecond while pixels with photons from multiple particles have most of these photons arriving within about one to a few nanoseconds – while the whole camera typically sees photons spread out from a few nanoseconds to 10s of nanoseconds, for large off-axis showers at large core distances seen in wide-field telescopes even beyond 100 ns.

The current generation of Cherenkov detectors is using analog memories and reading the signal at the same time for all pixels. Hence, either one has to read out a large buffer section of the analog memories or a significant amount of the signal is not recorded for some showers. The former would increase the dead-time and the latter would reduce the collection area. A compromise strategy is to have a so-called "sliding" readout window. A short readout time is used for all pixels, but the start of the readout is not made at the same time for all pixels. It follows the signal propagation within a camera. Possible real implementations of this readout scheme are being developed in the CTA consortium and these require the transmission of information of triggered pixels to the readout device of these associated pixels. These strategy will be implemented in the future full simulations to quantify their impact on the global performance of CTA.

### 9.4. Simulation of dual-mirror telescopes

While the simulation tools initially were restricted to telescopes with a single (segmented) reflector, they have been extended to include telescopes with secondary optics of the Schwarzschild–Couder (SC) design [6], of which two types are under development for CTA.

#### 9.4.1. Small Size Telescopes with secondary optics

Even though only Small Size Telescopes with Davies–Cotton (DC) optics have been simulated on a large scale so far (Table 1), proposals have also been made for the use of even smaller telescopes of the 3.5–4 m class, using secondary optics following the SC design to cover the high energy regime of the array. Such a telescope could be significantly less expensive due to the lower price per pixel for the photosensors available at the reduced plate scale of the SC optics, allowing more SSTs to be built, resulting in both improved angular resolution and effective area at high energies.

Of course with such an untested telescope design detailed simulations must be performed to try and quantify their effect on the performance of the array. Preliminary simulations have shown improvements can be made to the array effective area, while hav-
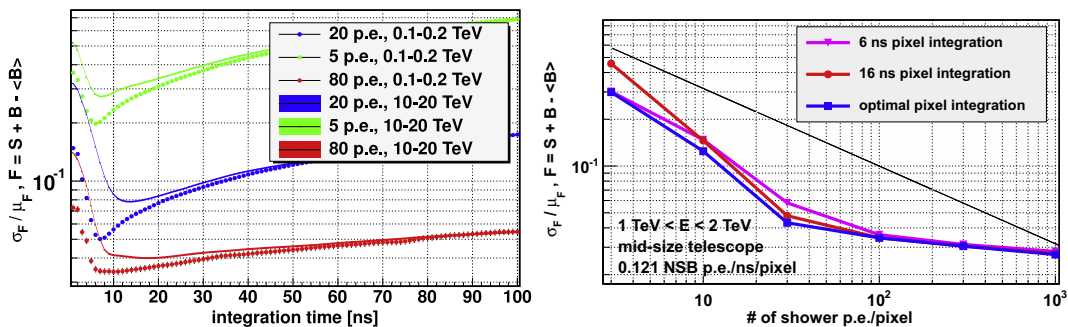


**Fig. 19.** Relative error on the integrated charge by mid-size telescope pixels: (left) as a function of the integration time, for the indicated signal p.e. charges, and (right) as a function of the number of shower p.e. per pixel, for two fixed and one dynamic integration windows (see text). The error represents the ratio standard deviation/mean of the distribution of the functional $F = S + B - \langle B \rangle$, where S, B and $\langle B \rangle$ are signal, NSB, and the average NSB (0.121 p.e./ns/pixel, dark sky) contributions. Note that the unavoidable $1/\sqrt{N_{pe}}$ Poisson fluctuations in the number of registered p.e.s are not included but shown separately (straight black line) and dominate in all cases shown here.
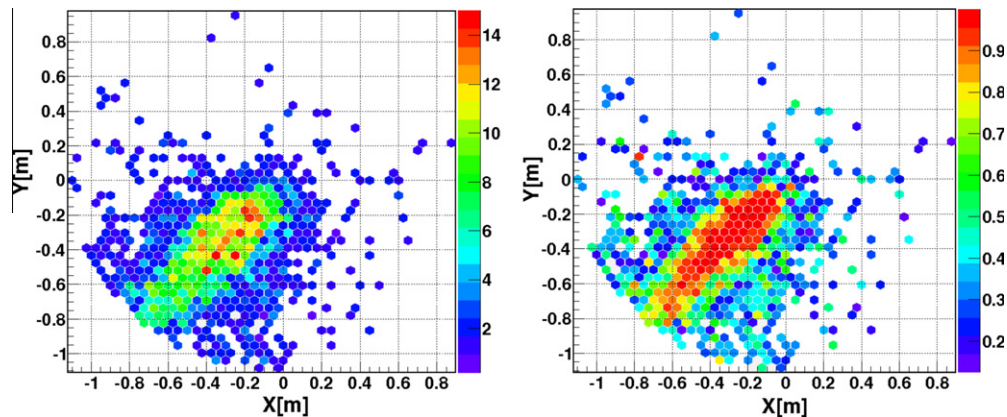
**Fig. 20.** (left) Focal plane distribution of the optimal pixel integration time values (ns), for a 49 TeV gamma-ray event with 133 m impact parameter. (right) For the same event, distribution of the fractions integrated/total signal charge. Only pixels with an actual Cherenkov signal in the simulation are shown.

ing little effect on the angular resolution. Larger scale simulations are planned, aimed at accurately determining the telescope performance (including background discrimination ability), as well as finding the optimum array layout.

In addition to these large scale simulations, simulations of specific aspects of the SC-SST designs are required, for example to quantify the performance of different photosensor/electronics combinations, such as multi-anode PMTs (MAPMTs) and silicon photomultipliers (SiPMs).

### 9.4.2. Schwarzschild–Couder Mid Size Telescopes

Continuing work begun by the AGIS Collaboration, which joined with CTA in September 2010, the US groups are leading an effort to develop two-mirror mid-size telescopes of SC optical design, and planning to extend the initial DC-MST array of about 20 telescopes by an additional 36 SC-MSTs. With O(60) telescopes, the MST array will fully enter the event-containment regime, where the effective area within the array is comparable to, or greater than, the effective area around the array's edges. This is an important advance over current arrays of 2–4 telescopes, for which the effective area is dominated by events that land outside the array (for example, only 5% of 1 TeV gamma rays land within the $10^4$ m$^2$ footprint of the VERITAS array). Contained events are much better sampled, providing improved background rejection (more likely to pick up anisotropies in hadronic showers), improved angular resolution (triangulation of the shower direction is much more effective when the shower is viewed from several widely spaced azimuthal angles), and reduced energy threshold (containment implies that the shower's impact distance to the several nearest telescopes will be less than the 100–200 m telescope spacing) [60,7].

The baseline SC-MST optical design has a ~9.5 m diameter primary mirror (4.4 m central hole), 5.4-m diameter secondary mirror, and a 5.6 m focal length, providing ~50 m$^2$ of effective light collecting area. The SC design offers several advantages over the DC design which become especially important for a large array. The SC optical design corrects for spherical and comatic aberrations and is optimized to minimize astigmatism, keeping the optical PSF smaller than the size of a pixel out to 4–5° off axis and providing a short focal length compared to DC-MSTs with a similar field of view. Increasing the field of view increases the telescope multiplicity of each event [61]. The demagnifying secondary mirror reduces the plate scale of the focal plane: an 8° field of view requires only a focal plane of 0.8 m diameter, providing a large reduction in per-channel costs for focal-plane instrumentation by enabling the use of, for example, 64-channel multi-anode PMTs. The small plate scale also makes it economical to reduce the angular size of each pixel from the ~0.15° used in current-generation

telescopes to ~0.07°, which is expected to significantly improve angular resolution [61]. The SC design also has no wavefront distortions, allowing tighter requirements on trigger timing, which ought to reduce the rate of accidental triggers at a given threshold and may allow operation at a lower energy threshold. Finally, the small plate scale and opportunity to use multi-channel photodetectors improves the modularity and serviceability of the focal plane instrumentation and data acquisition electronics.

Several challenges are introduced by the SC design, and a major thrust of the simulations effort will be to study trade-offs between cost and performance to refine the specifications for the SC telescopes. Aspects under study include

- The field of view and spacing of the telescopes, which impacts the number of channels of focal plane instrumentation required and the quality of the optical PSF at the edge of the field.
- The quality of the optical PSF across the field of view and angular size of the pixels, which again speaks to the number of channels required, as well as requirements on the mirror alignment precision and the optical quality of the aspheric mirror segments.
- The mechanics of the focal plane, including the accuracy to which pixels need to be placed across the curved focal plane, tolerances for optical cross talk and dead spaces between pixels, and whether light concentrators provide a benefit.
- The impact of vignetting on the optical design specifications and performance of the analysis of Cherenkov images near the edge of the field of view.
- Requirements on the slew speed of the telescopes, driven by gamma-ray burst follow-up.
- Studies of various options for triggering electronics to evaluate trade-offs between maximizing rejection of accidental and cosmic-ray triggers, maximizing the low-energy effective area, and minimizing costs. These studies will also impact the specifications for the data acquisition electronics, in particular setting the dead-time and throughput specifications.
- An evaluation of the overall impact of adding 36 SC-MSTs to the 23 planned DC-MSTs on the sensitivity, angular resolution, and energy threshold of the MST array.

## 10. Conclusions and outlook

We could demonstrate that current shower and telescope simulation methods agree well with each other and with measured data, verifying the simulation tools in use. After first large-scale simulations have shown that the initial goals for the CTA sensitivity are quite reasonable over most of the anticipated energy range,

the current simulation data sets have resulted in a number of array layouts which can satisfy the expectations for most physics goals and in a number of layouts more focused on individual science cases. The benefits of the huge improvement in performance by CTA with respect to the current generation of instruments are demonstrated in other papers of this journal issue. Only at the very lowest energies, the initial assumptions on a CTA sensitivity curve could not be fully met, due to fluctuations in hadron showers resulting in gamma-like background events and because the background distribution over the f.o.v. cannot be known perfectly (inclusion of background systematics in the analysis). In its core energy range, the initial expectations for CTA can be met if not surpassed. At the highest energies, the development of more cost-effective small telescopes may well result in effective areas well exceeding initial plans.

The analysis methods for an instrument like CTA are still under development, having achieved quite some improvements over the baseline method which is based on only the traditional Hillas parameters. While this development will continue it is important to see that a CTA layout optimal with one analysis method is also close to optimal with other methods. Our iterative procedure in optimizing the CTA layout and configuration can thus continue with a superset of near-optimal layouts, plus perhaps some borderline cases, in its next round. Together with improved cost estimates, this should provide the basis for an optimal CTA performance for almost any of the CTA astrophysics or fundamental physics goals.

## Acknowledgements

## References

[1] http://www.cta-observatory.org.
[2] W. Hofmann, M. Martinez, this issue.
[3] http://www.mpi-hd.mpg.de/HESS/.
[4] http://www.magic.mppmu.mpg.de/.
[5] http://veritas.sao.arizona.edu/.
[6] V. Vassiliev, S. Fegan, P. Brousseau, Astropart. Phys. 28 (2007) 10.
[7] CTA Consortium, Design concepts for the Cherenkov Telescope Array, Exp. Astr. 32 (2011) 193.
[8] C. Baixeras et al., 2004. Available from: <arXiv:astro-ph/0403180>.
[9] A. Konopelko, Astropart. Phys. 24 (2005) 191.
[10] F.A. Aharonian et al., Astropart. Phys. 15 (2001) 335.
[11] W. Hofmann, J. Phys. G: Nucl. Part. Phys. 27 (2001) 933.
[12] W. Hofmann et al., Astropart. Phys. 12 (1999) 135.
[13] G.P. Rowell et al., Nucl. Instrum. Meth. A 588 (2008) 48.
[14] A.V. Plyasheshnikov, F.A. Aharonian, H.J. Völk, J. Phys. G 26 (2000) 183.
[15] P. Colin, S. LeBohec, Astropart. Phys. 32 (2009) 221.
[16] V. Stamatescu et al., Astropart. Phys. 34 (2011) 886.
[17] I. de la Calle Pérez, S.D. Biller, Astropart. Phys. 26 (2006) 69.
[18] K. Bernlöhr et al., in: Proc. 30th ICRC, Mérida, vol. 3, 2008, p. 1469.
[19] V. Bugaev et al., in: AIP Conference Proceedings, vol. 1085, 2008, p. 834.
[20] D. Heck, J. Knapp, J.N. Capdevielle, G. Schatz, T. Thouw, Report FZKA 6019, 1998, Forschungszentrum Karlsruhe. <http://www-ik.fzk.de/corsika/physics_description/corsika_phys.html>.
[21] W.R. Nelson, H. Hirayama, D.W.O. Rogers, SLAC-0265.
[22] K. Bernlöhr, Astropart. Phys. 30 (2008) 149.
[23] M.P. Kertzman, G.H. Sembroski, Nucl. Instrum. Meth. A 343 (1994) 629.
[24] P. Vincent et al., in: Proc. 28th ICRC, Tsukuba, vol. 5, 2003, p. 2887.
[25] K. Bernlöhr et al., Astropart. Phys. 20 (2003) 111.
[26] R.D. Parsons et al., Astropart. Phys. 34 (2011) 832.
[27] A. Fassò et al., Report CERN-2005-10, 2005; Computing in High Energy and Nuclear Physics 2003 Conference (CHEP2003), paper-MOMT005; <arXiv:hep-ph/0306267>; <http://www.fluka.org>.
[28] S.A. Bass et al., Prog. Part. Nucl. Phys. 41 (1998) 225; M. Bleicher et al., J. Phys. G: Nucl. Part. Phys. 25 (1999) 1859.
[29] N.N. Kalmykov, S.S. Ostapchenko, A.I. Pavlov, Nucl. Phys. B (Proc. Suppl.) 52B (1997) 17.
[30] S.S. Ostapchenko, Nucl. Phys. B (Proc. Suppl.) 151 (2006). 143, 147.
[31] S.S. Ostapchenko, Phys. Rev. D 74 (2006) 014026.
[32] R. Engel et al., in: Proc. 26th ICRC, Salt Lake City, vol. 1, 1999, p. 415.
[33] J. Guy, Thèse de doctorat, Université Paris VI, 2003.
[34] P. Majumdar et al., in: Proc. 29th ICRC, Pune, vol. 5, 2005, p. 203.
[35] S. Funk et al., Astropart. Phys. 22 (2004) 285.
[36] R. Cornils et al., Astropart. Phys. 20 (2003) 129.
[37] F. Aharonian et al., (H.E.S.S. Collaboration), Astron. Astroph. 457 (2006) 899.
[38] F. Aharonian et al., (H.E.S.S. Collaboration), Astrophys. J. 664 (2007) L71.
[39] A.M. Hillas, in: Proc. 19th ICRC, vol. 3, 1985, p. 445.
[40] A. Daum et al., (HEGRA Collaboration), Astropart. Phys. 8 (1997) 1.
[41] V.P. Fomin et al., Astropart. Phys. 2 (1994) 137.
[42] R.W. Lessard et al., Astropart. Phys. 15 (2001) 1.
[43] T.-P. Li, Y.-Q. Ma, Astroph. J. 272 (1983) 317.
[44] D. Berge, S. Funk, J. Hinton, Astron. Astroph. 466 (2007) 1219.
[45] http://www.root.cern.ch
[46] A. Moralejo et al. (MAGIC Collaboration), in: Proc. 31st ICRC, Łódź, 2009, Available from: <arXiv:0907.0943>.
[47] J. Albert et al., (MAGIC Collaboration), Nucl. Instrum. Meth. A 588 (2008) 424.
[48] R.D. Parsons, Towards a Measurement of the Cosmic Ray Electron Spectrum at the Highest Energies, Using the Next-Generation Cherenkov Array CTA, Ph.D. thesis, University of Leeds, 2011.
[49] J. Hinton, The Electron Muon and Cherenkov Components of Extensive Air Showers Studied at the South Pole, Ph.D. thesis, University of Leeds, 1998.
[50] A. Hoecker et al., TMVA – Toolkit for Multivariate Data Analysis with ROOT, 2007. Available from: <arXiv:physics/0703039v4>.
[51] M. Lemoine-Goumard, B. Degrange, M. Tluczykont, Astropart. Phys. 25 (2006) 195.
[52] Y. Becherini et al., Astropart. Phys. 34 (2011) 858.
[53] Y. Becherini et al., Advanced analysis and event reconstruction for the CTA Observatory, in: F. Aharonian, W. Hofmann, F.M. Rieger (Eds.), Proc. 5th International Symposium on High-Energy Gamma-Ray Astronomy (Gamma2012), Heidelberg, July 2012, AIP Conference Proceedings, in press.
[54] Y. Shikaze et al., Astropart. Phys. 28 (2007) 154.
[55] O. Adriani et al., Phys. Rev. Lett. 106 (2011) 201101.
[56] M. Ackerman et al., (Fermi LAT Collaboration), Phys. Rev. D 82 (2010) 092004.
[57] B. Wiebel-Sooth, P.L. Biermann, H. Meyer, Astron. Astrophys. 330 (1998) 389.
[58] J. Beringer et al., (Particle Data Group), Phys. Rev. D 86 (2012) 010001 (Section 26).
[59] CTA Consortium, Contributions to the 32nd ICRC, Bejing, 2011, Available from: <arXiv:1111.2183>.
[60] G. Maier et al., in: Proc. 31st ICRC, Łódź, 2009, Available from: <arXiv:0907.5118>.
[61] V. Bugaev et al., in: Proc. 31st ICRC, Łódź, 2009. <http://icrc2009.uni.lodz.pl/proc/pdf/icrc0793.pdf>.